JPL PUBLICATION 82-39

Designing Dual-Plate Meteoroid Shields — A New Analysis

Hallock F. Swift
Robert Bamford
Ralph Chen

March 1, 1982

National Aeronautics and
Space Administration

Jet Propulsion Laboratory
California Institute of Technology
Pasadena, California

JPL PUBLICATION 82-39

Designing Dual-Plate Meteoroid Shields — A New Analysis

Hallock F. Swift
Robert Bamford
Ralph Chen

March 1, 1982

NASA
National Aeronautics and
Space Administration

Jet Propulsion Laboratory
California Institute of Technology
Pasadena, California

The research described in this publication was carried out by the Jet Propulsion Laboratory, California Institute of Technology, under contract with the National Aeronautics and Space Administration.

PREFACE

The senior author of this report, Mr. Hallock F. Swift, is President of Physics Applications, Inc., Dayton, Ohio. The work described in this publication was carried out under the auspices of the Applied Mechanics Division as part of the Halley Intercept Mission Project at the Jet Propulsion Laboratory, California Institute of Technology, under Contract No. NAS 7-100, sponsored by the National Aeronautics and Space Administration.

ACKNOWLEDGEMENTS

The authors would like to thank many staff members of the Jet Propulsion Laboratory for their ideas and helpful suggestions which contributed materially to the success of the reported project.

Special thanks are due to Dr. Jack Barengoltz of the JPL Staff for his suggestions regarding evaluating plasma temperatures during debris cloud stagnation processes and to Dr. Neil Divine who reviewed sections of the manuscript that describe the history, makeup, trajectories, and radiation response of comets in general and Comet Halley in particular.

ABSTRACT

Dual-plate meteoroid shields consisting of sacrificial bumper plates spaced some distance outboard from the vehicle hull are the most effective structures yet conceived for protecting space vehicles from meteoroid impacts. This report presents the development of a new analysis for designing dual-plate shields. The analysis is based upon energy and momentum conservation, fundamental electromagnetic radiation physics, and observation of results from extensive experimental impact investigations conducted at relatively lower velocities (near 7 km/s). One important conclusion is that most of the kinetic energy of a meteoroid striking a dual-plate shield is expended as radiation at the stagnation zone on the face plate of the underlying structure and that this fraction increases rapidly with increasing velocity. The analysis provides quantitative estimates of shield strength against four threats: blast loading of the underlying structure; direct impact of the underlying structure by meteoroids passing through holes in the bumper; impacts of the underlying structure from debris spalled from the bumper; and impacts from debris projected behind impacted hard points.

The analysis was developed during the Comet Halley Intercept Mission (HIM) study for protecting the spacecraft from the intense comet meteoric environment. The results have been generalized so that they are usable for: developing space vehicle protection against generalized meteoroid threats; developing meteoroid protection for vehicles dedicated to other cometary missions; and extending our understanding of impact mechanics at velocities well above those that have previously been considered in detail.

Included are also several other studies related to the shield design effort for the HIM vehicle. These studies were conducted to: consider designs for mirrors exposed to the dust environment; evaluate ion fields created by dust impacts on the vehicle shield; and consider the use of fiber composite materials to replace metallic shield components.

TABLE OF CONTENTS

LIST OF FIGURES

LIST OF TABLES

LIST OF SYMBOLS

A = Shield area opened by meteoroid perforations.

$\mathring{A}$ = Avogadro's number $\mathring{A} = 6.02 \times 10^{23}$ molecules/gm mole.

B = Ratio of the debris cloud wall thickness to its radius.

C = Energy per unit mass that can be absorbed by crushing honeycomb core material (for typical aluminum honeycomb $C = 5$ kJ/kg.

$\overline{C}_p$ = Material heat capacity at constant pressure averaged over the temperature span under consideration.

c = Velocity of light; $c = 3.0 \times 10^8$ m/s.

d_{bl} = Ballistic limit thickness.

E_e = Kinetic energy associated with radial expansion of the debris cloud.

E_k = Kinetic energy of the local sandwich structure.

E_m = Meteoroid kinetic energy.

E_r = Residual energy between meteoroid kinetic energy and kinetic energy associated with rearward motion of the cloud c.g.

e = Electronic charge; $e = 1.6 \times 10^{-19}$ Coul.

e_a = Maximum directed kinetic energy per atom/molecule of the debris cloud material.

e_c = Kinetic energy of the debris cloud per unit surface area when the cloud first contacts the stagnation surface.

e_{cr} = Energy required to crush completely a unit presented area of honeycomb core.

e_p = Photon energy.

e_h = Instantaneous on-axis kinetic energy per unit area of the face plate of an underlying structure.

e_k = Kinetic energy of rearward shield movement.

F = Cumulative fluence of meteoroids larger than a critical size.

G = Ratio of bumper hole diameter that contributes material to the debris cloud to meteoroid diameter.

H = Lagrangian boundary constraint factor.

h = Planck's constant; $h = 6.63 \times 10^{-34}$ WS^2.

J = Lagrangian parameter.

K = Ratio of mass per unit area of the bumper to that of the meteoroid.

k = Boltzmann's constant = 1.38×10^{-23} $WS/^oK$.

M_m = Meteoroid mass.

M_s = Equivalent local sandwich structure mass.

M_{mo} = Meteoroid mass for failing optimized shield.

m = Molecular weight of debris cloud material.

m_c = Mass per unit area of the debris cloud wall.

N_h = No. of meteoroids that will pass through holes in the bumper and fail the shield by perforation of the front face of the underlying structure.

N_{ho} = No. of meteoroids perforating the underlying plate of optimized shield design.

N_m = No. of meteoroids that will fail the shield by blast loading.

N_{mo} = No. of meteoroids capable of failing optimized shield by blast loading.

N_t = Total number of particles that can produce shield failure.

P_c = Momentum of the debris cloud per unit area on axis.

P_h = Honeycomb crushing pressure.

P_{hd} = Peak pressure on axis at stagnation surface.

P_m = Shield failure probability from blast loading.

P_t = Total shield failure probability.

P_2 = Shield failure probability from meteoroid perforation of the front sheet.

p = Shield failure probability.

Q = Ratio of the kinetic energy of the debris cloud's outward motion to energy available from momentum conservation.

R = Ratio of impactor kinetic energy to crater volume in an extensive target.

r_c = Impact crater radius (depth).

r_h = Final bumper hole radius.

r_m = Meteoroid radius.

S = Ratio of impact crater diameter to meteoroid diameter.

t_b = Bumper thickness.

t_{bo} = Optimized bumper thickness.

t_c = Thickness of honeycomb core.

t_h = Thickness of the front face of the underlying structure.

t_{ho} = Thickness of optimized front face of underlying honeycomb structure.

t_3 = Thickness of the rear surface of the sandwich panel.

t_{20} = Optimized thickness of the front honeycomb surface.

U_c = Rearward velocity of a debris cloud's c.g.

U_h = Velocity of the front face of the underlying structure on-axis.

U_m = Meteoroid velocity.

U_s = Local sandwich structure recoil velocity.

U_{max} = Maximum debris cloud velocity.

U_{min} = Minimum debris cloud velocity.

W = Momentum multiplication factor ($2 > W > 1$).

W_b = Bumper weight per unit area of the trial design.

W_{bo} = Optimized weight per unit area of the bumper.

W_{co} = Weight per unit area of optimized honeycomb core.

W_p = Weight per unit area of honeycomb core of the trial design.

W_t = Total shield weight: total power radiated per unit surface area.

W_2 = Weight per unit area of the front face of the underlying structure of the trail design.

W_3 = Weight per unit area of the rear sandwich surface of the trial design.

W_{20} = Optimized weight per unit area of the front face of the underlying structure.

W_{30} = Optimized weight per unit area of the rear surface of the honeycomb sandwich.

w = Black body power radiated per unit surface area per unit wavelength span.

w_c = Mechanical power input per unit area to stagnation zone on axis; weight per unit area of honeycomb core of trial design.

w_t = Power radiated per unit area.

X = Spacing between bumper and protected structure.

X_o = Optimized spacing between the bumper and underlying structure.

x = Maximum distance of the debris cloud (on axis) behind the bumper.

x_{50} = Material thickness required to absorb 50% of incident radiation.

β_m = Slope of the cumulative meteoroid fluence vs. meteoroid size curve at the design meteoroid size.

β_b = Slope of the cumulative meteoroid fluence vs. meteor size curve at the size needed to just perforate the bumper.

β_h = Slope of the cumulative meteoroid fluence vs. meteor size curve at the size needed to just perforate the front face of the underlying structure.

ε = Surface emissivity.

ϕ = Angle subtended by expanding debris cloud from the bumper.

$\Delta\theta$ = Temperature of stagnated debris cloud material over R.T.

δX = Displacement of front honeycomb sandwich face.

θ = Temperature.

θ_o = Room temperature.

ν = Photon frequency.

λ = Lagrangian multiplier: wavelength.

λ_m = Wavelength where radiation intensity is maximum.

ρ_c = Honeycomb core density.

ρ_d = Areal density of stagnated debris material.

ρ_h = Density of the front face material of the underlying structure.

ρ_m = Density of meteoroid material.

ψ = Material scattering/absorption cross-section.

ξ = Size scaling ratio needed to achieve meteoroid shield optimization.

τ_c = Time for forward cloud segment on axis to stagnate.

η = Ratio between total shield mass and thickness of the front face of the sandwich for the trial design.

η_o = Ratio between total shield mass and thickness of the front face of underlying shield of the optimized design.

1. INTRODUCTION AND BACKGROUND

This report describes results of a series of investigations conducted to evaluate means for protecting a large spacecraft from meteoric environments. One particular intense environment is that associated with a close encounter with Halley's Comet. The protection problem is especially complex because of the very large impact velocities produced by the relative velocity vectors between Halley's Comet and vehicles launched into relatively low energy encounter orbits from Earth.

1.1 INTRODUCTION

Vehicle trajectories planned for the Halley's Intercept Mission (HIM) vehicle as it encounters Halley's Comet would carry the vehicle through an intense veil of meteoric material. Halley's Comet is unusual in that it travels in its orbit around the Sun retrograde to most other objects. As a result, encounters between the HIM vehicle on a low energy orbit from Earth and Halley's Comet occur at velocities ranging from 62 km/s to 72 km/s depending upon the time chosen for the encounter during the middle Spring of 1986. These encounter velocities are much higher than can be studied experimentally using laboratory accelerators of macroparticles. They are also considerably above impact velocities considered in detail using theoretical tools during previous studies of meteoric impacts with spacecraft. The potential for disastrous encounters due to the enormous impact velocities is obvious.

An effort was initiated at the Jet Propulsion Laboratory (JPL) during late 1979 to increase understanding of supervelocity impacts (impacts at speeds above 20 km/s) and to develop design methodologies for specifying meteoroid shields that would have high probabilities for protecting the Halley's Intercept Mission (HIM) vehicle during its encounter with Halley's Comet. Other JPL studies have provided reasonably precise estimates of the meteoroid environment (1,2). The activities reported in this document concern establishing the physics governing meteoric impacts with the HIM spacecraft and several of its critical components exposed to the meteoroid flux.

Important individual activities of this effort include:

- Developing a physical understanding of the interaction between supervelocity meteoroids and dual-element meteoroid shields.
- Developing methodologies for designing dual-element shields to provide specified protection levels at minimum weight.
- Studying related phenomenology concerning vehicle interactions with the Halley meteoroid environment including: impact erosion of outboard mirrors exposed to the meteoroid flux; ion fields resulting from meteoric impacts with the HIM vehicle; and use of fiber-reinforced plastics as substitutes for metallic shield materials.

The emphasis for all of these activities has been placed upon solving problems associated with the HIM vehicle encountering Halley's Comet. Where possible, the results have been generalized so that they are usable for: developing space vehicle protection against generalized meteoroid threats; developing meteoroid protection for vehicles dedicated to other cometary missions; and extending our understanding of impact mechanics at velocities well above those that have previously been considered in detail.

1.2 BACKGROUND

1.2.1 Comets

Comets are fascinating objects for astronomical investigation because they are among the most primitive bodies associated with the solar system. As such, they provide one of the best sources available for information concerning the early phases of solar system development. Comets are probably bodies made up of ice (primarily water ice, but also ices of carbon dioxide, ammonia, and methane) into which is embedded numerous agglomerations of silicate crystals. A substantial number of these "dirty snowballs" reside in space beyond the known planets of the solar system. Occasionally, combinations of stellar and planetary gravity perturbations work together with solar

gravity to cause an individual comet to plunge into the inner solar system along a nearly parabolic orbit which takes it through the inner solar system and returns it to deep space beyond. As the comet approaches the Sun, the resulting intense radiation sublimes away part of the ice surface and releases the nonvolatile silicate debris. Much of this debris is lofted slowly away from the comet by gasdynamic drag induced by the exiting gaseous material. This solid material then effectively flies in formation with the comet itself for extended periods until it finally defuses away. Meanwhile, the evolved gas streams away from the comet in directions approximately opposite to the Sun due to the effect of radiation pressure and solar wind. The visible comet tails and the less spectacular comet anti-tails are made up of ions and dust particles, respectively.

Occasionally an incoming comet passes close enough to one of the principal planets (Jupiter, Saturn and possibly Uranus or Neptune) to dissipate significant amounts of its kinetic energy in the moving planetary gravity field. This energy reduction traps the comet in an elliptical orbit about the Sun whose aphelion distance may vary over wide ranges. These comets make repeated passes by the Sun which may or may not produce spectacular displays from the vantage point of Earth.

The meteoric material produced during multiple encounters of the comet with the Sun tends to become spread out roughly along the cometary orbit and produce the well-known terrestrial meteor showers, as these orbits are encountered by the Earth several times per year.

1.2.2 Halley's Comet

The best known and among the most spectacular of all comets is Halley's Comet whose apparitions have been traced back historically to more than two millennia B.C. It is believed to be an ice block near 3 km in radius which travels around the Sun with an orbital period of approximately 76 years. Perihelion distance is somewhat inside the Venus orbit and the aphelion lies somewhat beyond Neptune's orbit. Current estimates are that about 30% of the mass of

the comet is made up of siliceous particles. The parent material of these particles has a density near 2.3 g/cm^3, but the gross densities of the larger agglomerations are near 0.75 g/cm^3. The smallest crystals themselves have diameters between 0.1 and 0.5 μm and aspect ratios between 3 and 10. Thus, the gross densities of meteoroids emitted from Halley's Comet vary with meteoroid size. When sizes are typical of the individual crystals, densities are near 2.3 g/cm^3. These densities fall monotonically with increasing meteoroid size until they reach 0.80 g/cm^3 for meteoroids 1 mm in size and larger.

Halley's Comet produces as spectacular a display as almost any comet when the Earth is properly situated for observation. Nearly ideal observation conditions occurred during the apparition of 1910. The spectacular display was caused by the fact that Halley's Comet is unusually large and unusually prolific in its gas emission. An anti-tail (a apparent luminous protrusion toward the Sun) was photographed in 1910. Presence of the anti-tail demonstrates clearly that Halley's Comet is a rich source of large dust particles, which indicates strongly that Halley's Comet may be expected to possess an intense veil of such particles.

This veil represents an extreme danger to spacecraft sent along low energy orbits from Earth to encounter the comet during its passage near the Sun, because the impacts of meteoroids with the vehicle will be both numerous and extraordinarily violent due to their very large closure velocities.

Closure velocities between 62 and 72 km/s are expected (depending upon the time chosen for encounter) because Halley's Comet travels retrograde around the Sun so that its orbital speed must be nearly added to that of the probing vehicle. The relative velocity vectors between all meteoric material associated with Halley's Comet and the encountering vehicle are almost exactly that of the comet itself due to the relatively tiny velocity difference between the meteoroids and the comet body. For this reason virtually all material impacting a vehicle approaching Halley's Comet approaches

from a single direction so that meteoroid impact protection measures need be applied to only one side of the vehicle. Current understandings of the meteoroid flux field surrounding Halley's Comet have been incorporated into a computer code by Dr. Neil Divine of JPL[2]. This code has been used widely by many investigators to estimate the total meteoroid fluences experienced by vehicles as they encounter Halley's Comet.

1.2.3 Halley's Intercept Mission Vehicle

The vehicle envisioned by the Jet Propulsion Laboratory for intercepting Halley's Comet is a 3-axis stabilized platform with a presented area of 6.4 m^2. (See Figure 1.) It would be launched directly from Earth with a Titan rocket or from the Space Shuttle in Earth orbit and would follow a near minimum energy trajectory to encounter Halley's Comet shortly after perihelion which occurs on February 9, 1986. The vehicle was to carry a high performance camera for viewing the comet both from a considerable distance during approach where detailed navigational and ephemeris information would be acquired and during encounter where photographs of the cometary surface would be recorded. The original vehicle configuration would also carry other instruments to observe radiation from the comet over wide spectral ranges and to determine the chemistry of both gaseous and solid material emitted from the comet. The chemistry experiments dictated that an absolute minimum of material be emitted from the vehicle itself and that this material be limited chemically to constituents not expected to be present in the comet itself.

A later configuration of the HIM vehicle replaced almost all of the observing instruments except the camera with a system for collecting meteoric and gaseous material emitted by the comet and sealing this material into a pod which would be returned to Earth several years after the encounter when the HIM vehicle was again in near-Earth space. The cometary material would then be recovered for analysis to determine cometary chemistry.

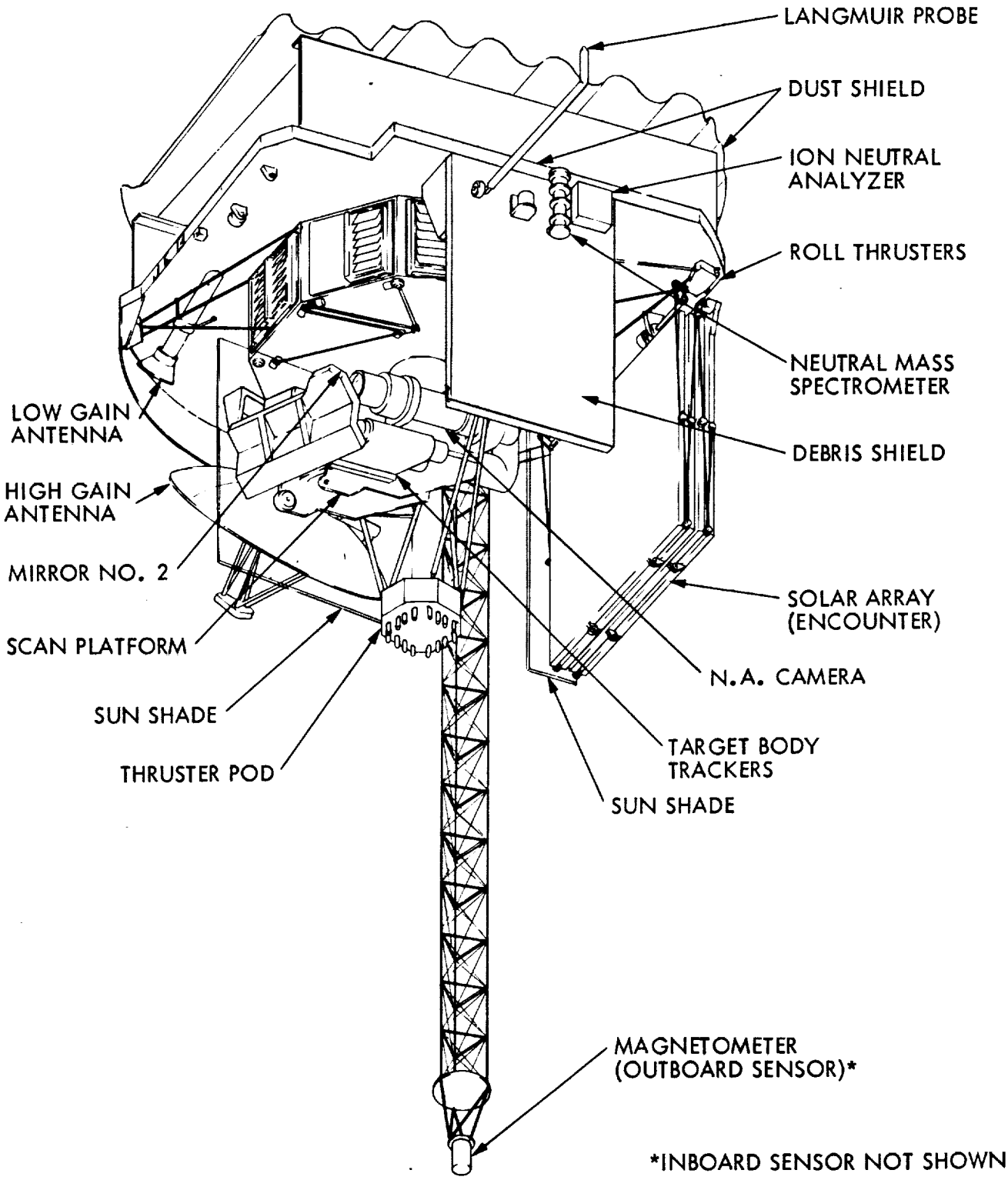

Figure 1. Sketch of Proposed Halley Intercept Mission (HIM) Vehicle. The Corrugated Meteoroid Bumper Appears at the Top.

1.3 REPORT STRUCTURE

The remainder of this report is divided into three chapters which describe specific phases of the research program.

- Chapter 2 contains a description of supervelocity impacts between meteoroids and 2-layer meteoroid shields.
- Chapter 3 presents design methodologies for specifying meteoroid protection armor.
- Chapter 4 describes a variety of supporting activities conducted during the research program.

2. PHYSICS GOVERNING ULTRA HIGH VELOCITY IMPACTS ONTO DUAL-PLATE METEOR ARMOR

By far the most important problems for analyzing meteoroid protection measures for the HIM vehicle involve establishing the physics governing supervelocity impacts against dual-plate meteoroid shields. Let us start our discussion of this subject with a qualitative description of such an impact process, and continue by developing specific quantitative models for the individual processes.

2.1 QUALITATIVE OPERATION OF DUAL-PLATE METEOROID SHIELDS

A dual-plate meteoroid shield consists of a thin plate (bumper) spaced a considerable distance in front of the surface to be protected. An incoming meteoroid strikes the bumper and is shattered. The impact perforates the bumper allowing a majority of meteoroid and bumper debris to be projected rearward behind the bumper. This material expands transversely as it proceeds rearward producing a thin-walled bubble of debris. The bubble finally impacts the surface to be protected over an extended area. The area increase of the secondary impact over that of the primary one reduces sharply local impact intensity. Impacts against dual-plate meteoroid armor have been studied experimentally at velocites up to 7.5 km/s. Weight savings of more than a factor of ten have been demonstrated experimentally during these studies for dual-plate meteoroid armor configurations compared with homogeneous metal armor with the same protection capability.

The analyses described in the remainder of this chapter must be exercised to demonstrate their operation and to provide numerical information for justifying a variety of simplifying assumptions. We have specified a single impact situation for carrying out all of these analyses which is detailed in Table 1. The values for the dimensionless ratios G, Q, and B have been chosen somewhat arbitrarily to reflect results of experiments conducted at velocities near 7.0 km/s and our current understanding of supervelocity impacts.

PARAMETER	SYMBOL	VALUE
• Incoming Meteoroid Mass	M_m	10^{-4} kg (0.1 gm)
• Nominal Impact Velocity	U_m	7 X 10^4 m/s
• Impact Kinetic Energy	E_m	245 kJ
• Molecular Wt. of Debris Cloud material	m	20 kg/kg mole (20 g/g mole)
• Spacing Between Bumper and Cloud Stagnation Surface	X	0.30 m
DIMENSIONLESS RATIOS		
• Bumper Mass/Unit Area vs Meteoroid Mass/Unit Area	K	0.25
• Dia. of Bumper Hole Contributing to Debris Cloud vs. Meteoroid Dia.	G	1.0
• Energy of Cloud's Outward Motion vs. Energy from Momentum Conservation	Q	1.0
• Cloud Wall Thickness vs. Cloud Radius	B	0.20

Table 1. Specification of a Standard Impact Typical of One That Might be Experienced by the HIM Vehicle.

2.2 NATURE OF METEOROID DISRUPTION PROCESS

Extremely intense shockwaves are produced in both the oncoming meteoroid and the bumper material at the instant of initial contact. These shockwaves propagate rearward into the oncoming meteoroid and forward into the bumper. The pressures immediately behind the shockwaves are enormous when meteoroid impact velocities in the range of 60 - 70 km/s are considered.[9] Typically these pressures exceed one-terrapascal (10 megabars). The material is also heated to temperatures between 5×10^5 °K and 5×10^6 °K. Densely confined material at these temperatures can radiate away its internal energy at rates up to $3.5 \times 10^{15} W/m^2$. This energy loss potential will be shown shortly to produce negligible energy transfer to radiation at the original impact site.

The shockwaves propagate at supersonic speeds (with respect to the unshocked material) forward into the bumper material and rearward into the meteoroid material after initial contact. This motion continues until the waves reach free surfaces at the rear of the bumper and at the sides and rear of the meteoroid. It is a fact of nature that a free surface cannot withstand normally-directed stress components.[10] This condition is met at free surfaces upon which shockwaves impinge by instantaneous production of releasewaves whose localized tensile stress is precisely opposite the instantaneous compressive stress of the oncoming shockwave thus canceling to zero the normal stresswave component at the surface. These releasewaves propagate in the opposite direction to the shockwaves that produce them or back into the shocked material where they relieve the pressure back toward zero. Temperatures also fall back to values somewhat above the pre-shocked situation and most of the energy originally stored in the material behind the shockwave is converted to directed kinetic energy as the material is accelerated to high velocity.

Let us now consider the problem of radiation from the material shocked by the original impact. Initially, no energy radiated by the shocked material can escape because it is surrounded by cool (unshocked) material that is almost completely opaque to the

radiation. Radiative energy starts to leave the shocked material when the shockwave moves close enough to a free surface so that the radiation being emitted behind it can penetrate the remaining material and reach the space beyond. Typically this penetration occurs when the shockwave is within 1 μm from a free surface or less. The releasewave produced when the shockwave reaches the free surface quickly terminates radiation as an important mechanism for energy transfer by cooling the shocked material to the point where extreme radiation intensities are no longer possible. Thus, we have a surface with dimensions roughly similar to the original meteoroid (no larger than a few mm in diameter) radiating for a period roughly equal to the time required for a shockwave to make a dual transit through 1 μm of material (typically a few tens of picoseconds). While the source may be extraordinarily bright, the flash duration and the source area limit the total energy transfer to a negligible value. A maximum of 10 joules can be emitted by a standard impact (Table 1) whose total kinetic energy exceeds 200 kJ.

Let us now consider the state of material during and after passage of the original (primary) shockwave. The normal stresses produced by the shockwave (greater than 1 terrapascal) are orders of magnitude greater than any conceivable material strength which assures that material motion under the influence of the shockwaves is affected negligibly by material strength. The state of material in the shocked condition is difficult to define since neither its density nor its shape is governed by materials properties. (We might almost consider the material to be a gas.) Intense shockwaves add entropy to the material through which they pass.[10] The amount of entropy added becomes almost proportional to peak shock pressure with the proportionality constant being governed largely by the material's shock compressibility. Material release from high pressure is nearly an isentropic process, on the other hand, so that entropy transferred to the material by shockwave transit is trapped. This entropy appears as internal energy (heat) when the material returns from its shock-compressed state. The material returns in solid form (although

massively disrupted) if this "entropy heating" provides less internal energy than the material's fusion energy. The material appears as a liquid if the entropy heating provides more energy than the material's fusion energy but less than its sublimation energy, and it returns as a gas if the sublimation energy level is exceeded. Table 2 lists the impact conditions required to melt and vaporize a number of metals via entropy heating. This tabulation shows clearly that all material subjected to the primary shockwaves from impacts at the speeds considered here (60+ km/s) are vaporized regardless of their shock compressibilities or sublimation energies. The states of materials in debris clouds will be shown later to have a profound effect upon subsequent phases of the impact processes.

A number of experimental investigations conducted at impact velocities below 7.5 km/s have shown that the critical parameter for determining the combined disruption efficiency of projectile and bumper material in the cloud behind an impacted bumper is the ratio, K, between the masses per unit presented area of the bumper and projectile.[5,6,7] A ratio of K = 0.25 was shown to produce the most complete material disruption (and the least-lethal debris clouds) when these clouds consisted principally of solid fragments, liquid droplets, or gas. Additionally, this criterion of K = 0.25 appears to be valid for describing bumper impact computations using numerical finite-difference routines when impact velocities throughout the meteoroid impact regime have been investigated.[9] Accordingly, we assumed that this criterion is valid in the supervelocity impact regime of interest and have applied it to the analysis described here.

Meteoric impacts with too thin bumpers do not necessarily cause materials involved to vaporize or even melt regardless of impact velocity. When the meteoroid is larger than the shield is designed to protect against, a shockwave propagates through the bumper after impact to the rear surface where it initiates a releasewave that propagates back through the bumper into the projectile and overtakes the primary shockwave in the projectile before it can shock all the

projectile material. The releasewaves are dispersive so they do not eliminate the ongoing shockwave completely at initial contact. Rather, they cause severe shockwave attenuation that reduces stresses sharply at positions immediately beyond the original shockwave-releasewave enounter. The result of such a situation is that some meteoric material is not fully shocked and may pass through the bumper into the space behind it without being affected fully. This impact situation is of no direct interest to the problem at hand since it represents impact conditions beyond those the protected vehicle is expected to survive.

A similar and much more common situation occurs when the bumper is too thick. This situation occurs often during a vehicle mission because it involves meteoroids smaller than those for which the shield was optimized impinging upon the bumper. In this case, a shockwave that propagates into the projectile is reflected by interactions with the side and rear walls. Resulting releasewaves propagate forward and overtake the primary shockwave in the bumper before this wave reaches the rear surface. Bumper material is then projected toward the vehicle hull without being fully shocked and, therefore, may propagate as liquid droplets or even solid fragments.

We can use this line of reasoning to argue that solid bumper material will always be projected behind bumpers exposed to real meteoroid fluxes because these fluxes always contain relatively large numbers of particles smaller than the largest particles protected against. In general, meteoroid populations contain sizes down to those that can just perforate the bumper and smaller ones that can only crater the bumper. Impacts from many of these particles meet the too-thick bumper criteria discussed above and lead to solid bumper material being projected toward the hull.

Let us consider these solid bumper fragments in more detail because they may represent a threat to the overall shield protection under some circumstances. The shockwaves that create and launch these fragments are strongly divergent spacially due to the geometry of the impact process between a tiny meteoroid and a relatively thick

plate. Since the locally-induced motion of the bumper material produced by passage of the shockwave and releasewave is normal to the local wave surface, large gradients in direction are produced in the resulting velocity fields. These gradients tear the bumper material apart as it is projected behind the impacted bumper. The fineness of this material disruption is controlled by the toughness of the bumper material in withstanding velocity gradients within individual fragments. The material of an individual fragment must dissipate the kinetic energy associated with separation motions within it through elastic and plastic deformation if it is to remain a single particle.

We propose a conservative specification for the maximum size of solid debris fragments projected energetically behind an impacted bumper: the largest fragments have equivalent spherical diameters equal to the bumper thickness.

Solid particles projected behind bumpers are launched by a single shockwave encounter. As such, their velocities are limited to twice the particle velocity associated with the shockwave [10] which, in turn, is determined by shock stress level. Shockwave stress levels also control the heat added to material via entropy heating described earlier. Thus, maximum velocities may be assigned to solid material projected behind impacted bumpers depending upon the shock and thermal properties of the bumper material. Shockwaves with particle velocities near 2.5 km/s will just melt aluminum (see Table 2) which indicates that solid aluminum fragments may be shock-accelerated to velocities no higher than approximately 5 km/s.

Thus, we have a model that establishes both the maximum size and velocity of fragments launched behind impacted bumpers in terms of the geometry of the bumper and physical properties of bumper materials.

2.3 PERFORATION OF METEOROID BUMPERS

Many experimental studies have indicated that holes produced in bumper plates by projectile impact are up to several times the

diameter of the impacting projectile. [4,5,6] It was thought originally that essentially all the material from such holes participated in the energetic debris plumes projected behind impacted bumper plates. Later, more careful investigations have shown this not to be the case (at least for impact velocities below 7.5 km/s). The only bumper material observed in energetic debris clouds behind impacted bumpers comes from the area of the bumper under the projection of the projectile onto the surface. The remainder of the material in the hole appears to be projected laterally along the bumper surface. It is either piled up in lips around the final hole or moves off at low speeds in directions nearly parallel to bumper surface.

The hole diameters are significant to overall shield operation because these holes provide free access to the protected elements of the structure for subsequent meteoroids. Thus, the probability of a particle large enough to penetrate the unprotected second surface passing through holes in the bumper without touching the bumper wall must be less than the failure probability budget if the shield is to operate effectively (should a small meteoroid touch any portion of the bumper while passing through it, the meteoroid would be shattered completely and its lethality to the second plate would be reduced sharply).

A variety of empirical relationships have been proposed for predicting hole diameters produced by meteoroids perforating bumpers. These data represent interpolations and extrapolations of experimental results gathered at velocities up to 7.5 km/s and their extrapolation to the velocities of current interest (near 70 km/s) produces preposterous results. Equation 1 from Reference 6 is an example of such an equation that reflects the most recent experimental data available.

$$r_h = 4.5 \times 10^{-5} \, r_m \, U_m \, (t_b/2r_m)^{2/3} + 0.9 \, r_m \qquad (1)$$

Where: r_h and r_m = radius of bumper hole and meteoroid respectively; U_m = meteoroid impact velocity; and t_b = bumper plate thickness. Applying this formulation to the standard impact situation produces the result that the hole produced by a 3 mm dia. meteoroid is nearly 100 mm in diameter!

We propose a model for predicting bumper hole sizes more realistically based upon hole sizes produced by several limiting impact situations.

Both basic theoretical arguments [11] and experience indicate that projectiles traveling at any velocity passing through membranes whose thickness is a negligible fraction of characteristic projectile dimensions produce a hole that accurately reflects the projection of the projectile onto the surface, i.e., the hole size is the same as that of the projectile. Another extreme situation occurs when the projectile size is reduced to the point where it can just perforate the bumper, (i.e., the ballistic limit size) where we may assume that the hole diameter has just reached zero.

An intermediate point occurs where the projectile produces a maximum-diameter hole. We have chosen to set an upper limit for this diameter equal to the diameter of a crater that would have been produced if the projectile impacted a thick block of bumper material. The size of this crater can be estimated at least approximately by application of the principles that the volume of an impact crater is proportional to the kinetic energy of the impactor and that hypervelocity craters are nearly hemispherical. Applying these two criteria produces a relationship between projectile and crater diameters and impact conditions presented in Equation 2.

$$r_c = r_m \left(\frac{\rho_m U_m}{R} \right)^{1/3} \qquad (2)$$

Where:

r_c and r_m = the radius of the crater and meteoroid respectively;

ρ_m and U_m = the gross density and velocity of the meteoroid, respectively; and R is the proportionality constant relating meteoroid kinetic energy to crater volume (typical values of R for stoney materials impacting aluminum are near $R = 10^9$ J/m^3 (10^{10} erg/cm^3). Evaluating this relationship for a meteoroid with gross density of ρ_m = 0.75 tonne/m^3 (0.75 gm/cc) and a velocity of $U_p = 7 \times 10^4$ m/sec yields a ratio of crater diameter to meteoroid diameter of $S = r_c/r_m = 12.2$. This value, according to the model, is the maximum hole size that can be expected in an impacted bumper. We assume further that the bumper thickness required to produce such a hole is half the crater radius (or depth), i.e., a maximum diameter performation is produced when the deepest penetration of a crater in a block is twice the thickness of the bumper.

The ballistic limit thickness has been shown by numerous studies (experimentally at velocities up to 7.5 km/s and theoretically at higher speeds) to be approximately 1.5 times the crater depth in a thick plate (or 18.3 times the projectile radius for the case considered here).

These three points are plotted in Figure 2. We have no information available on how they are to be connected and so we propose to use straight lines point-to-point to represent the currently most probable values. We have also shown the more conservative "constant value" fit for smaller-than-optimum meteoroids, which we choose to take as the worst-case situation.

This analysis is sufficient for establishing an upper bound on the hole sizes produced in bumper plates by meteoroid impacts. It is almost certainly conservative so that its use in analysis of bumper shield effectivess should introduce an inherent safety factor.

Material	Melting				Vaporization			
	Incipient		Complete		Incipient		Complete	
	Pressure Mb	Al Impact Velocity km/sec	Pressure Mb	Al Impact Velocity km/sec	Pressure Mb	Al Impact Velocity km/sec	Pressure Mb	Al Impact Velocity km/sec
Magnesium	0.48	5.40						
Aluminum	0.70	5.60	1.00	7.0				
	0.67	5.50	0.88	6.6	1.67	10.2	4.70	
	0.61	5.10	0.85	6.5				
Titanium	1.30	7.60						
Iron (Steel)	1.80	7.90	2.10	8.80				
Cadmium	0.33	2.50	0.46	3.20				
	0.40	3.0	0.59	3.9	0.88	5.2	1.80	8.1
	0.33	2.5	0.43	3.15	0.70	4.4	5.30	
Copper	1.40	6.60	1.84	8.00				
	1.40	6.60	1.84	8.00	3.40	12.6	34.00	
Nickel	2.3	9.00						
Lead	0.25	2.00	0.35	2.60				
	0.27	2.1	0.34	2.5	0.84	4.8	2.30	9.1

Table 2. Shock and Impact Conditions Required to Create Phase Changes in Selected Shocked Materials.

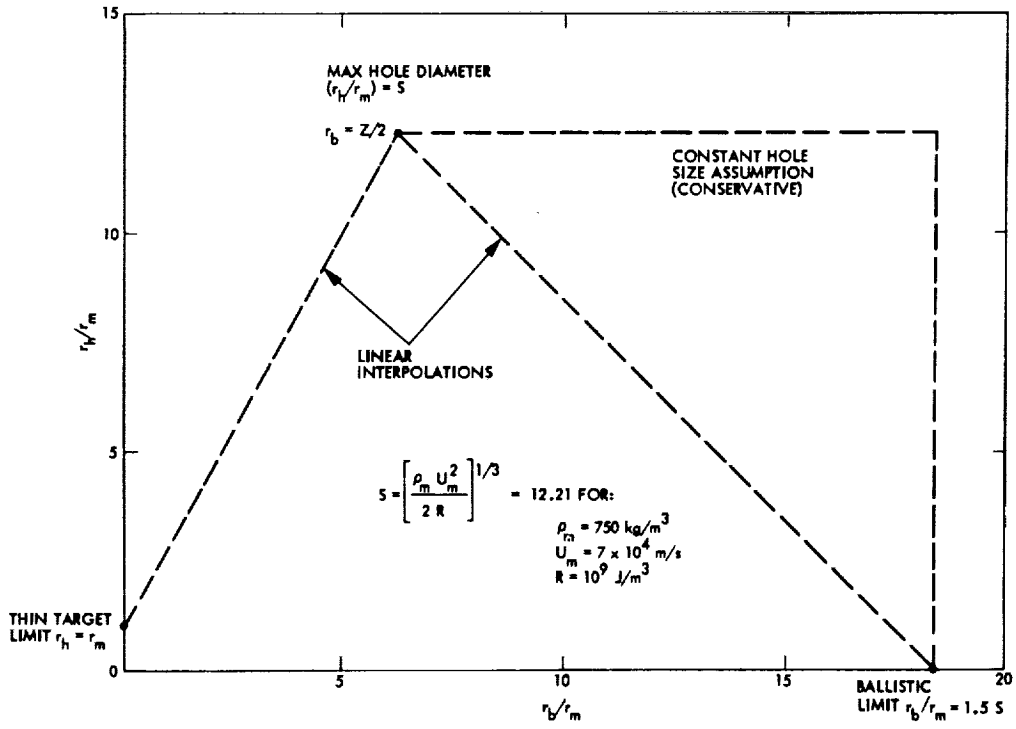

Figure 2. Plot of Hole Diameter in a Meteoroid Bumper vs. Bumper Thickness Both Normalized With Respect to Meteoroid Size. The Plot Represents Results of the Proposed Hole Size Model With Two Options for Estimating Hole Sizes Produced by Small Meteoroids.

2.4 EXPANSION OF DEBRIS CLOUDS BEHIND IMPACTED BUMPERS

Experiments conducted at velocities of 7.0 ± 0.5 km/s have shown that debris material exiting behind an impact site on a bumper expands transversely as it proceeds rearward to form a debris bubble (see Figure 3). These bubbles were found to be basically empty regardless of the physical state of the debris material (solid, liquid, or gas). Debris clouds of solid and liquid fragments tended to fill less than 2% of the internal space.[16] Gaseous debris clouds may fill as much as 10% - 15% of this space.[16] We see no reason that impacts at velocities near 70 km/s should change the physics of the situation enough to affect this empty-cloud observation significantly. Accordingly, the remainder of the analysis incorporates the assumption that the ratio of instantaneous cloud thickness to cloud radius, B, is well below unity.

We have chosen to consider the debris expansion process as an explosion caused by the impact of the meteoroid with the bumper material immediately beneath it. This choice was inspired by an analysis of bumper armor operation suggested originally by A. J. Richardson.[21] The center-of-gravity (c.g.) of the debris plume moves rearward from the bumper (toward the vehicle hull) according to conservation of linear momentum. The material making up the plume expands away from the c.g. as a spherical shell where all material travels outward at a single speed.

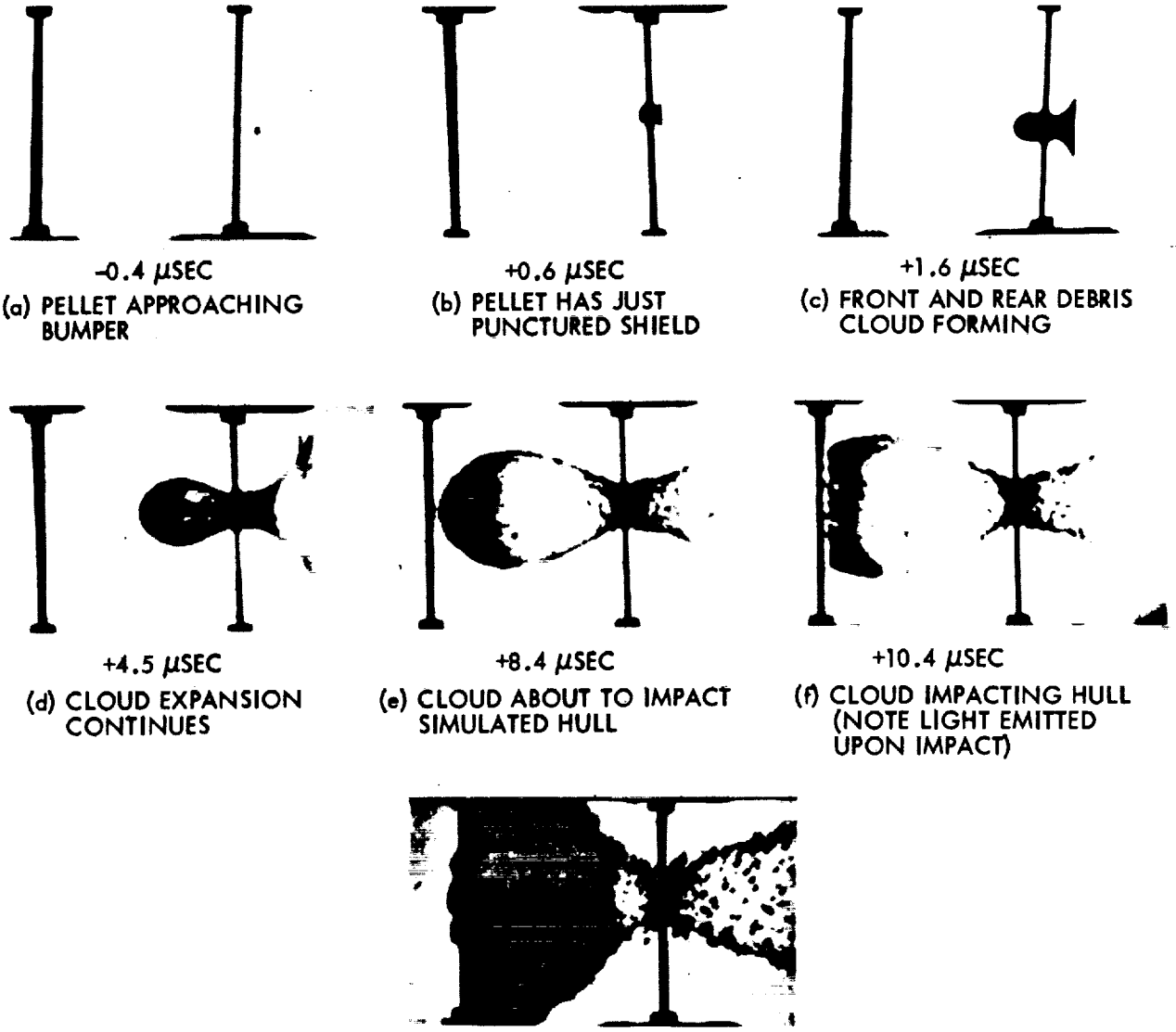

Figure 3. Development of a Debris Plume Produced by a 3MM Aluminum Sphere Impacting a 0.75 MM Thick Aluminum Plate Simulating a Meteoroid Shield at a Velocity Near 7.0 Km/s. The Images are Selected From a Cine' Sequence Taken at a Rate Near 10^6 pps. Note That Cloud Material Becomes Luminous After Being Stagnated on the Second (Hull) Plate (Frame f) and Rupture of the Second Plate shown in Frame (g).

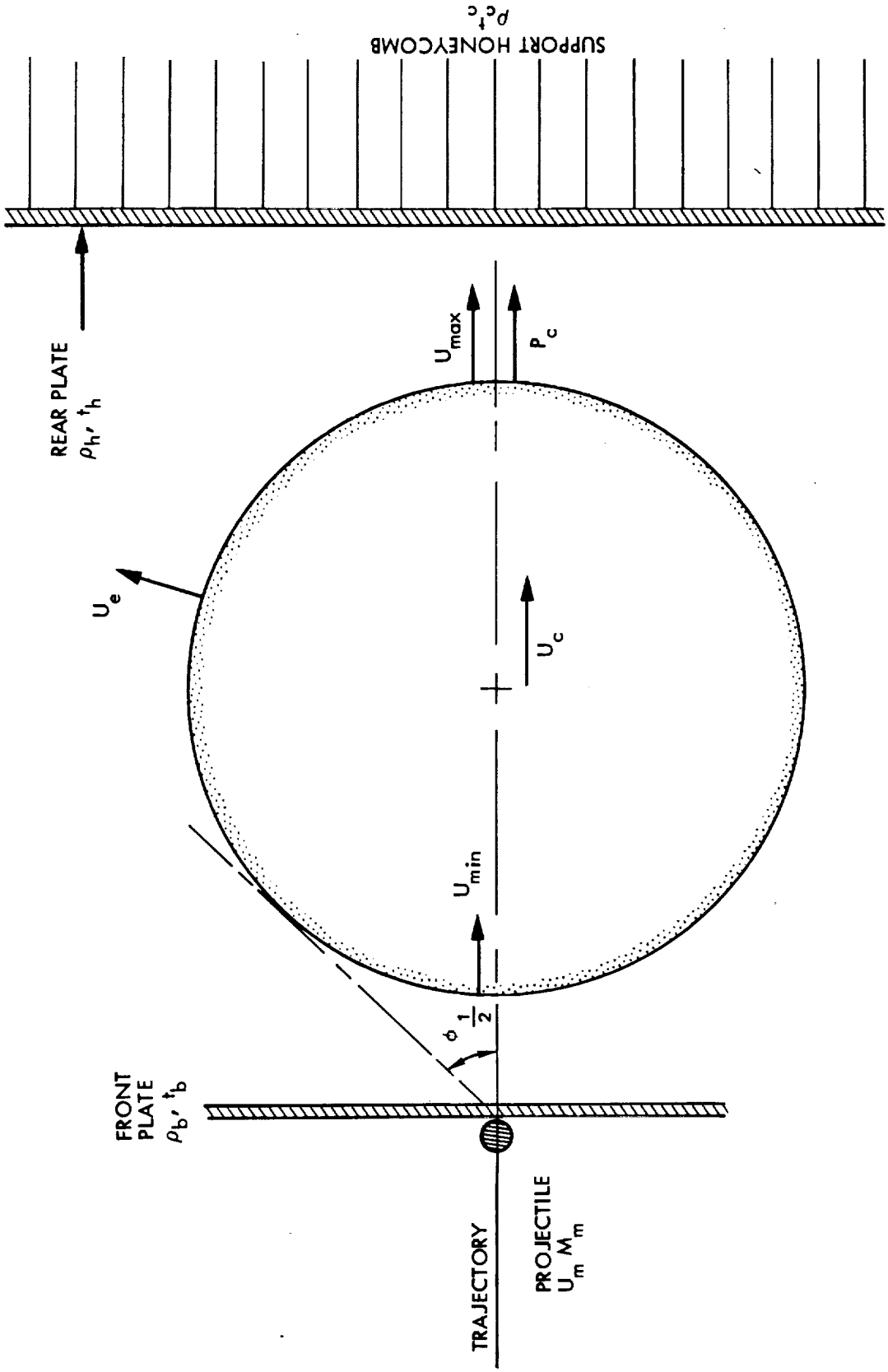

Figure 4. Sketch of Debris Cloud Expanding Behind an Impacted Bumper Presenting Selected Parameters Used in the Analysis.

The debris cloud expansion process is diagrammed in Figure 4. Note that most surface points on the rear plate are struck by both the front and rear segments of the spherical debris shell. On-axis, the rear cloud surface will be shown later to travel at, typically, 30% of the velocity of the front surface (and contain, typically, 10% as much specific energy). Off-axis, the intensity of forward cloud parameters as seen from the stagnation plate falls with increasing angle from the axis as measured from the impact point. The intensity of the rear cloud parameters increase with angle off-axis at comparable rates. Very roughly, these two factors offset one another Total cloud impingement parameters on the stagnation surface are maximum on axis, but they reduce to a markedly small degree with increasing off-axis angle. For computational simplicity, we have chosen to make all calculations for the on-axis case only and to leave to specialized analyses the more mathematically complex exercises needed for complete evaluation of the models proposed.

Let us start a quantitative treatment of this process by evaluating the velocity of the c.g. of the debris plume, U_c, in terms of the incoming projectile velocity, U_m, the ratio of the masses per unit area of the target plate and projectile, K, and the ratio of the diameter on the bumper which produces material for the energetic debris cloud to the projectile diameter, G. Note that experimental evidence indicates that G has a value near unity as discussed in Paragraph 2.3 of this report.

$$U_c = \frac{U_m}{1 + KG^2} \qquad (3)$$

Equation 3 was derived by setting the momentum of the incoming projectile equal to the momentum of the debris cloud which consists of the projectile and target material participating in plume formation.

Inherent in this derivation is the assumption that insignificant material (and momentum from the impact process) is projected into the debris plume emanating from the front surface of the bumper. Efforts to measure this front-projected momentum at impact velocities near 7 km/s indicate that its value is less than 1% of the momentum of the incoming projectile.

We also assume that no momentum is transferred to the bumper plate itself. This assumption corresponds with both experimental measurements at light-gas gun velocities and general experience and is also easy to justify by considering that momentum can only be transferred from the impact site to the remainder of the plate via shear stress whose amplitude is limited by material strength. The time during which this impulse can be transferred is limited to the time required for the impact to occur (roughly approximated by the time required for the original projectile to pass through the bumper plate unimpeded). Such durations typically under 0.5 μs and are always less than 1 μs for impact situations of interest here so that total impulse transferrable to the plate is effectively limited to 0.1% or less of the total input momentum.

Conservation of momentum as evaluated in Equation 3 leads to a net reduction in the kinetic energy of the final system (conservation of linear momentum which is proportional to the first power of incoming velocity is not consistent with conservation of energy which is proportional to the velocities squared). We can evaluate the energy loss E_r in terms of the original kinetic energy E_m of the projectile and the dimensionless ratios, K and G previously defined.

$$E_r = E_m \left(\frac{KG^2}{1 + KG^2} \right) \qquad (4)$$

This lost energy E_r is that which is available to drive all of the phenomena associated with thin-plate impact processes other than the motion of the c.g. of the debris plume. Specifically, this

energy equals the total of: kinetic energy associated with debris projected in front of the bumper plate; thermal and kinetic energy transferred to the the bumper; energy radiated from the impact site when the shocked material is at high temperature; trapped thermal energy in the debris (entropy heating); and kinetic energy of the debris cloud associated with its outward expansion from the c.g. We have presented a number of arguments earlier in this report to indicate that all of these energy sinks except for the last one are small compared to the last one, i.e., a sustantial majority of the energy available through momentum conservation is expended as kinetic energy of the debris material expanding away from the c.g. We are not convinced, however, that the total of these other energy sources can be ignored completely. For this reason, we have assigned a factor, Q, as the ratio of the energy expended as kinetic energy of the debris expansion to the total available energy. The factor, Q, should have a value near but below unity in subsequent equations.

We are now in a position to evaluate the expansion velocity of material in the debris plume away from the c.g., U_e, since we know the total mass of the debris and the kinetic energy associated with the expansion process. U_e has been evaluated in Equation 5 in terms of the original projectile velocity U_m and the dimensionless ratios G, K and Q defined earlier.

$$U_e = \frac{U_m \, G \sqrt{QK}}{1 + KG^2} \qquad (5)$$

We may now define the angle subtended by the expanding debris plume at the original impact site, ϕ. One-half of this angle, $\phi_{1/2}$, is proportional to the sine of the ratio of the expansion velocity U_e to the c.g. velocity U_c as is evaluated in Equation 6.

$$\phi_{1/2} = \sin^{-1} (G \sqrt{QK}) \qquad (6)$$

We can also calculate the maximum and minimum rearward velocities of the debris plume, U_{max} and U_{min} corresponding to motions of the front and rear of the debris bubble on-axis. Maximum and minimum plume velocities are evaluated with respect to the original projectile velocity as U_{max}, U_{min} respectively and the dimensionless ratios in Equation 7A and B.

$$U_{max} = U_m \left(\frac{1 + G\sqrt{QK}}{1 + KG^2} \right) \tag{7A}$$

$$U_{min} = U_m \left(\frac{1 - G\sqrt{QK}}{1 + KG^2} \right) \tag{7B}$$

Let us complete this phase of the discussion by developing expressions for the mass per unit area of the debris cloud during its expansion and its momentum per unit area. The mass per unit area of the cloud, m_c, is evaluated by calculating the cloud radius as impingement starts and dividing the equivalent spherical area into the total mass of the debris cloud as is accomplished in Equation 8.

$$m_c = \frac{M_m (1 + KG^2)(1 + G\sqrt{QK})^2}{4 \pi X^2 G^2 QK} \tag{8}$$

Evaluating m_c for the standard impact conditions described in Table 1 at the instant when the cloud first touches the rear plate ($x = X$) produces the result that $m_c = 6.63 \times 10^{-4}$ Kg/m^2 ($m_c = 6.63 \times 10^{-5}$ gm/cm^2). The equivalent thickness of aluminum at solid density

is 0.25 μm.

We can now evaluate the momentum intensity contained within the cloud on axis by multiplying twice the mass per unit area of the cloud at the instant of contact by the sum of the on-axis components of the expansion velocity, U_{max}, + U_{min}. This process has been carried out and the result is presented in Equation 9 where the momentum intensity of the debris cloud p_c is evaluated in terms of the mass and velocity of the incoming projectile M_m and U_m, respectively; the distance behind the bumper plate where impingement occurs, X; and the dimensionless ratios K, G and Q.

$$p_c = \frac{M_m U_m (1 + G \sqrt{QK})^3}{4 \pi X^2 G^2 QK} \qquad (9)$$

Evaluating Equation 9 for the standard impact parameters yields the result p_c = 149 NS/m^2 (p_c = 1490 taps*).

(* 1 tap = 1 dyne sec/cm^2)

2.5 DEBRIS CLOUD INTERACTION WITH UNDERLYING SURFACES

The rearward-directed momentum intensity of the debris cloud is transferred to the underlying structure upon which the cloud impinges. In principle, this momentum intensity may be increased by up to a factor of W = 2 if the incoming material rebounds from the impacted surface. Evidence from experimental studies at velocities of near 7.0 ± 0.5 km/s indicates that rebound is minimal. The authors decided to investigate this process in some detail because the impact situations considered for the Halley's Intercept Mission are so different from those examined experimentally.

Let us start the analysis by evaluating the mechanical power associated with the cloud stagnation process. This power input is the source of energy for heating the stagnated cloud material. The peak "kinetic power intensity" (peak mechnical power input to the stagnated material per unit area) may be estimated by calculating the

energy content per unit area of the leading surface of the debris cloud on-axis and dividing this value by the time required for the debris cloud to travel its own wall thickness. The peak kinetic energy of the cloud per unit surface area when it contacts the stagnation surface, e_c, is half the product of the mass per unit area of the cloud, m_c from Equation 8, and the maximum cloud velocity, U_{max} squared, from Equation 7A.

$$e_c = \frac{M_m U_m^2 (1 + G\sqrt{QK})^4}{8 \pi X^2 G^2 QK (1 + KG^2)} \qquad (10)$$

If we consider that debris clouds have wall thicknesses B times their radii, the time required for impingement of the leading surfaces of the cloud to occur on-axis becomes:

$$\tau_e = \frac{X B G \sqrt{QK} (1 + KG^2)}{U_m (1 + G\sqrt{QK})^2} \qquad (11)$$

The kinetic power, w_c, associated with cloud stagnation may now be evaluated by dividing Equation (10) by Equation (11) to produce Equation 12.

$$w_c = \frac{M_m U_m^3 (1 + G\sqrt{QK})^6}{8 \pi X^3 G^3 B (QK)^{3/2} (1 + KG^2)^2} \qquad (12)$$

Evaluating Equation 12 for the standard impact situation with the assumption that the debris cloud is 20% full (B = 0.2) produces an input power estimate of $w_c = 4.42 \times 10^{12}$ w/m^2 (4.42×10^8 w/cm^2).

We may now continue the analysis by considering the impact of the plasma plume with the stagnation surface. Evaluation of U_{max} using Equation 7 shows that the maximum velocity of the debris cloud

on-axis is somewhat greater than the original impact velocity over the range of interest to this study (the velocity U_{max} relative to the projectile velocity U_m has a maximum value of 1.2066 when the ratio, K, of bumper mass-per-unit-area to that of the projectile has a value of K = 0.191 and the other dimensionless parameters, G & Q are considered unity). Equation 7A and 7B are plotted in Figure 5.

The range of interest for this analysis extends from K = 0.1 to the limit of the analysis applicability which is estimated to be near K = 5-10. Thus, we may expect that the most severe point of the debris plume striking the underlying surface has a velocity between 100% and 120% of the incoming velocity (up to 84 km/s for the Halley's intercept mission when the incoming projectile velocity is near 70 km/s). The peak specific energy of this material (e_a in electron volts per atom) is evaluated in Equation 13 in terms of the electronic charge, e; Avogadro's number, Å; the molecular weight of the species of interest, m; and the peak impingement velocity, U_{max}.

$$e_a = \frac{5 \times 10^{-4} m U_{max}^2}{e \mathring{A}} \qquad (13)$$

The dominant materials in a debris cloud are expected to be: silicon with an atomic weight of 28 gm/mole; aluminum (from the bumper) with an atomic weight of 27 gm/mole; and oxygen with an atomic weight of 16 gm/mole (or molecular weight of 32 gm/mole). Evaluating Equation 13 using a somewhat arbitrary mean molecular weight of 27 gm/mole for the debris yields an average specific energy of 989 electron volts per atom (ev/atom) (36.6 ev/amu).

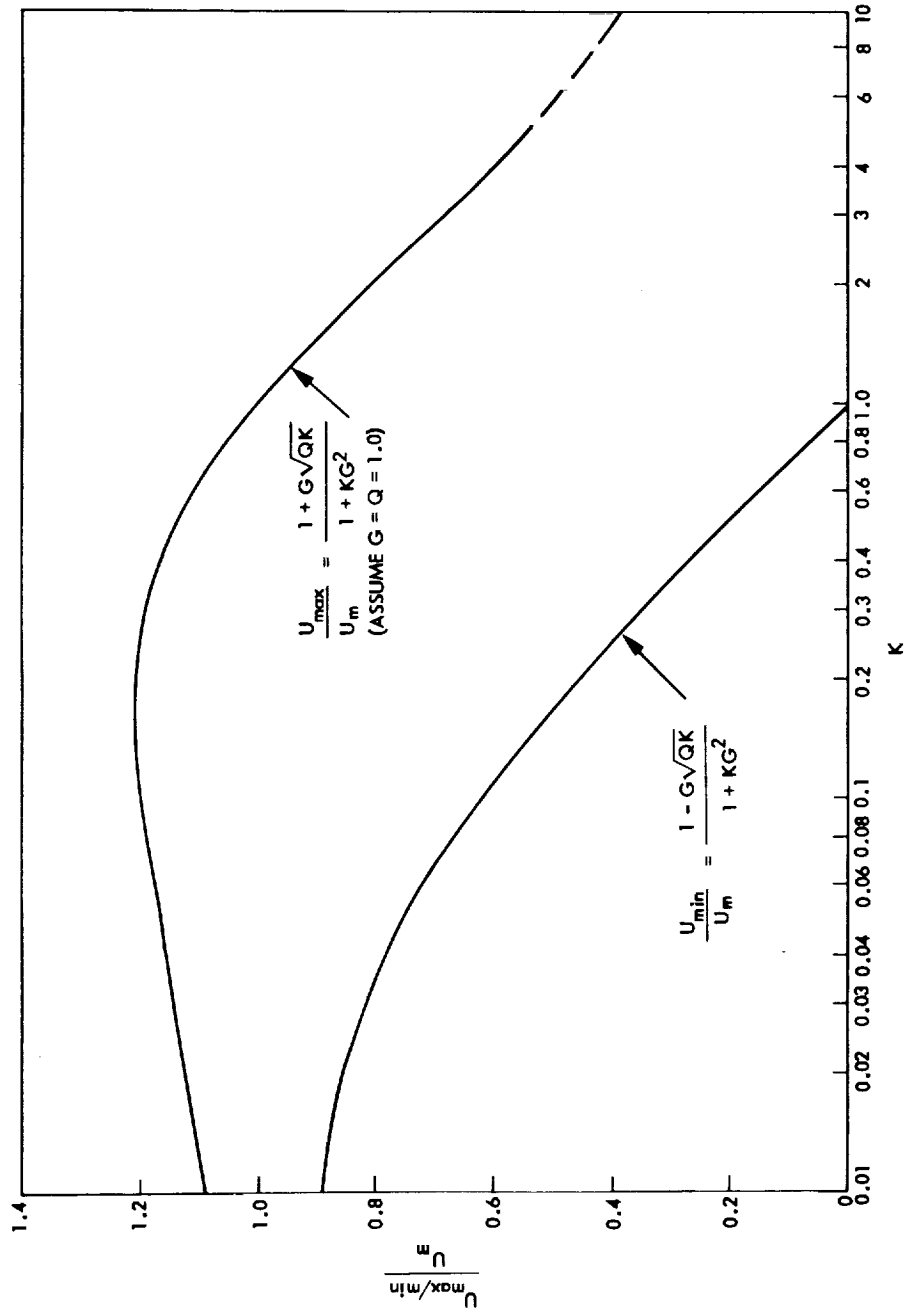

Figure 5. Plot of Maximum and Minimum Debris Cloud Velocity on Axis vs. the Ratio of Bumper to Projectile Areal Densities, K, Predicted by the Analysis.

Atomic and molecular beams of both electrically charged and uncharged particles traveling at these energies are able to penetrate significant distances (on the order of 250 nm) into metallic targets. We estimate, therefore, that the oncoming debris from a supervelocity impact actually enters the surface of the stagnating structure and gives up its directed kinetic energy to heat. We further estimate that rough thermal equilibrium is established between the constituents of the debris cloud and the material of the stagnation plate that is mixed with it during the penetration process. An example evaluated later in this discussion indicates that realistic shield designs for the Halley's intercept mission vehicle lead to rough parity between the material in the debris plume and the material from the stagnation plate which is mixed with it. If the stagnation plate is made principally from aluminum (high strength aluminum alloy), its mean molecular weight of 27 gm/mole will roughly match that of the debris cloud so that the energy available to the material will be roughly one-half of the incoming specific energy or 500 ev/atm.

Material with internal energy of 500 ev/atm is enormously hot! If we use the atomic physics concept that 1 ev = 12,000 ^{o}K, the predicted temperature would be 6 x 10^{6} ^{o}K. If, on the other hand, we calculate temperature increase, $\Delta\theta$, by assuming an average heat capacity for the material over the temperature range from room temperature to the expected value, we may use Equation 14 to express temperature increase in terms of parameters defined above and the average heat capacity for the material $\bar{C}_p$.

$$\Delta\theta = \frac{e_a \, e \, \mathring{A}}{\bar{C}_p} \qquad (14)$$

Assuming a rather conservative value of $\bar{C}_p$ of 28 kJ/kgm mol ^{o}K (0.25 cal/gm for m = 27 gm/mole) yields a temperature estimate of $\Delta\theta$ = 3.4 x 10^{6} K or slightly more than one-half of the previous estimate. A computation recently conducted to support the Giotto

vehicle mission to Halley's Comet where finite-difference computer analyses were used with the most up-to-date available models for the thermodynamic properties of silicates and aluminum led to an estimate of peak stagnation temperatures somewhat above 500,000 ^{o}K.(7)

Let us now consider the energy radiated from the hot material on the surface of the stagnation plate by making the trial assumption that the material is optically thick, i.e., the great majority of photons emitted from the underlying regions of this material are absorbed before they reach the front surface. This assumption will be checked later in the analysis. If the material is optically thick, we may assume safely that it radiates as a black (not gray) body. The radiation intensity with respect to spectrum, W_λ, may be evaluated in terms of black body temperature using Planck's Equation (15):

$$w_\lambda = \frac{2 \pi c^2 h}{\lambda^5} \left(e^{hc/k\lambda\theta} - 1\right) \qquad (15)$$

where: c = velocity of light = 3.00×10^{8} m/s; h = Planck's constant = 6.63×10^{-34} WS, K = Boltzmann's constant = 1.38×10^{-23} WS/ ^{o}K, λ = radiation wavelength in meters; and θ = black body temperature in ^{o}K.

This equation is somewhat cumbersome to use in its general form. It may be integrated over all radiation wavelengths to produce the Stefan-Boltzmann Equation which relates total power radiated per unit surface area at all wavelengths to temperature.

$$w_t = \varepsilon\sigma \left(\theta^4 - \theta_0^4\right) \approx \sigma (\Delta\theta)^4 \qquad (16)$$

The result is presented in Equation 16 where: ε = emissivity of the radiating surface ($\varepsilon = 1$); σ = the Stefan-Boltzmann's constant =

5.67×10^{-8} Wm^2; and θ_o = the temperature of the surroundings = O.

The wavelength at which radiation is emitted at maximum intensity is evaluated by differentiating Equation 15 with respect to wavelength and setting the derivative equal to zero in order to locate an extreme (maximum) value of the function. The result is Wein's displacement law presented in Equation 17.

$$\lambda_m = 2.9 \times 10^{-3}/\theta \qquad (17)$$

where λ_m is the wavelength (expressed in meters) at which the surface radiates at maximum intensity. If we evaluate Equation (16), assuming a gas temperature of 10^6 ^oK, the heated material is computed to radiate with a power density of 5.67×10^{16} W/m^2 (5.67×10^{12} W/cm^2). This radiation power level is approximately 12,800 times the peak kinetic power input to the stagnated material as calculated by Equation 12! The conclusion we may draw from this result is that the stagnated plasma radiates away the kinetic energy input to it from the stagnation process as fast as it is supplied if the plasma radiates as a black body and if the radiation escapes the local area.

The wavelength at which the radiation intensity is maximum (calculated from Equation 17 using $\theta = 10^6$ ^oK) is $\lambda_m = 2.9$ nm. The energy associated with these photons E_p may be evaluated using Equation 18:

$$e_p = \frac{hc}{e\,\lambda_m} \qquad (18)$$

where ν = photon frequency (H_z). The result is that the energy of the photons emitted at maximum intensity from the stagnated

material is 428 ev/atom.

We are now in a position to establish whether or not the stagnated debris material is optically thick with respect to its own radiation. This determination is made by estimating the range of 428 ev photons traversing debris cloud material. If this range is considerably shorter than the equivalent cloud thickness, the cloud material is optically thick and may be expected to radiate as a black body. If, on the other hand, the range is large with respect to the equivalent material thickness, the cloud is optically thin to its own radiation and may be expected to radiate as a gray body (i.e., emissivity, ε, from Equation 12 is significantly less than unity).

A detailed, experimental and theoretical treatment of the absorption cross-sections for all atomic species irradiated by photons with energies between 1 KV and 1 MV is presented in Reference 8. We have reproduced a graphical plot of this data for aluminum in Figure 6 and have extrapolated it from the minimum 1 KV photon energy to 100 volts. Indications from this curve are that aluminum atoms absorb 428 ev photons with a cross-section of approximately $\psi = 1.5 \times 10^5$ barns/atom (1.5×10^{-23} m^2/atom). A simple approximate equation for the penetration range of this radiation through dense stagnated plasma is presented as Equation 19.

$$x_{50} = \frac{3 \times 10^{-3} \text{ m}}{8 \rho_d \Psi \text{ Å}} \qquad (19)$$

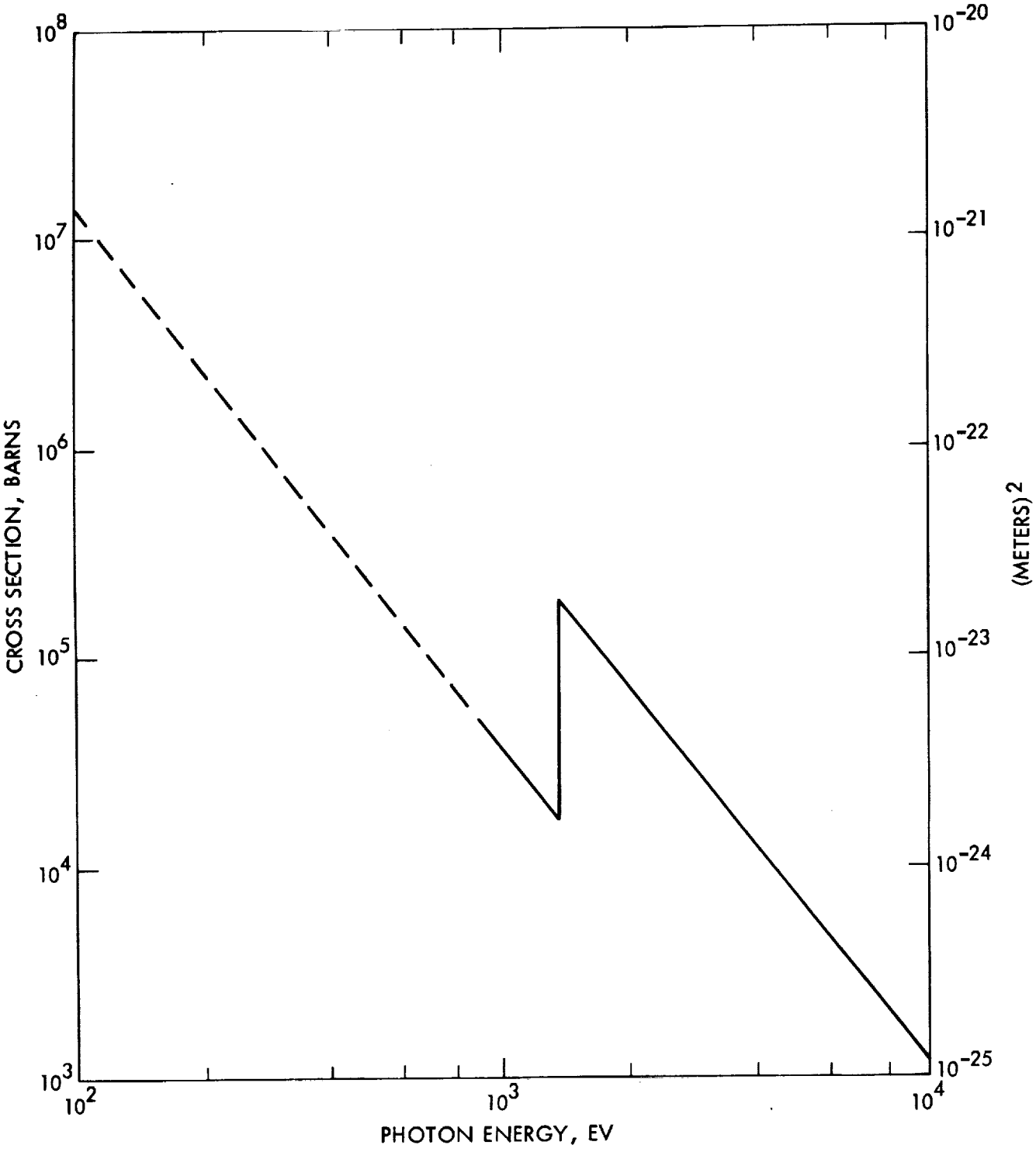

Figure 6. Plot of Atomic Scattering Cross Sections for Aluminum vs. Photon Energy. Note that the Dashed Portion of the Plot is an Extrapolation of the Results Reported in Reference 8

Where:

x_{50} is the range required to intercept 50% of the emitted photons; m is molecular weight of the plasma material (m = 27 gm/mol.); ρ is the material mass density (ρ = 2700 kg/m^3, 2.7 gm/cm^3; and $\mathring{A}$ is Avogadro's number ($\mathring{A}$ = 6.02 x 10^{23} atom/gm mol). Evaluating Equation 19 for an aluminum plasma compressed to solid density yields a photon range for 50% absorption of x_{50} = 413 nm. Since this range is somewhat less than 1/4 the anticipated thickness of the plasma sheath, we may expect the plasma to be optically thick to its own radiation and to radiate as a black body, thus, lending credence to the numerical values associated with the radiation analysis.

We should note here that this result (blackness of the plasma) is a function of original meteoric impact velocity. The temperature to which the plasma is heated upon stagnation may be expected to rise rapidly with increasing impact velocities. A point is reached at some impact velocity above 70 km/s where the energy of the photons radiated from the plasma at maximum intensity allows them to penetrate the full thickness of the plasma cloud without probable absorption. The plasma then ceases to be optically thick and estimating the radiation intensity from the stagnated plasma becomes considerably more complex. This process does not have a major impact on the final results, however, because half of the plasma radiation is always directed toward the stagnation plate where it must be absorbed. This energy absorption heats progressively larger amounts of the stagnation plate material due to increased radiation penetration of the more energetic photons and much of the irradiated material joins the stagnated plasma and comes into thermodynamic equilibrium with it thereby decreasing its temperature.

The facts that the photon range through the plasma is a significant fraction of the plasma thickness (greater than 20%) and that the plasma sheath is very thin indicate strongly that the plasma can maintain rough thermodynamic equilibrium with itself during the period when kinetic energy input is being radiated away through resorting to relatively mild levels of turbulence (random

material motion through the plasma sheath thickness). As this analysis is applied to progressively lower velocity impacts, the photon energy of the most intense radiation falls monotonically with decreasing velocity as does the penetration range of the radiation through the plasma itself. The plasma, thus, remains black and its surface radiation follows the conventional black-body radiation relationships presented earlier. Progressively larger levels of turbulence must be presumed to allow the plasma to maintain thermodynamic equilibrium through its thickness, which is required to assure that plasma radiation keeps up with kinetic energy input from the cloud stagnation process. Loss of thermal equilibrium within the plasma allows temperature gradients to develop so that the outer portions of the plasma can cool with respect to the remainder through radiating away part of its energy. Thus, radiation effectiveness as an energy removal mechanism falls as impact velocities are lowered.

This difficulty is exacerbated by the fact that the effectiveness of radiation for removing input power to the stagnation process falls rapidly with decreasing impact velocity. This situation may be investigated analytically by evaluating the ratio of radiated power from the plasma sheath as calculated by Equation (16) after substituting expressions for temperature from Equations (14) and (13) to kinetic input power to the plasma sheath (Equation 12). The result is presented in Equation (20).

$$w_t/w_c = \frac{5 \times 10^{-13}\ \pi\ \sigma\ m^4\ U_m^5\ X^3\ G^3\ B\ (QK)^{3/2}}{M_m\ \bar{C}_p^4} \frac{(1 + G\sqrt{QK})^2}{(1 + KG^2)^6} \quad (20)$$

The important factor to note in Equation 20 is that the original meteoroid impact velocity, U_m, appears raised to the 5th power! The line of argument presented here assumes that a lower velocity limit exists below which plasma from the stagnation regime cannot radiate away energy delivered by the stagnation process quickly enough to

prevent energy buildup. Under these conditions, the plasma may be expected to take up this excess energy as kinetic energy by re-expanding after stagnation and to provide momentum multiplication to the stagnation surface. It is of passing interest to note the velocity where the ratio of radiated power, to input power falls to unity ($W_t/W_c = 1$), for the geometry being considered is $U_m = 13.48$ km/s. This velocity happens to be near that required to just vaporize both meteoroid and typical metallic bumper materials under ideal impact circumstances.[12]

2.6 REACTION OF THE SECOND (PROTECTED) ELEMENT OF THE METEOROID SHIELD

Plasma from a bumper impact that impinges upon a second plate spaced behind the bumper transfers impulse to this plate so rapidly that the plate cannot respond significantly during impulse application (the classic impulse approximation). Under these conditions the surface of the plate is given a local out-of-plane velocity profile. The plate then responds to this velocity profile in a manner governed by structural considerations. Under extreme conditions, the plate may deform rearward rapidly until internal strains cause cracking and finally catastrophic rupture. At the opposite extreme, the plate may respond to the impressed velocity profile by deforming within its elastic limit as the impulse is transferred to the remainder of the structure and thus sustains no damage at all. Dynamic analyses describing response of complex structures to even simple impulse applications is a field only now being treated rigorously for realistic structures through use of dynamic, three-dimensional, finite-element structural analyses. Treatment of these situations is clearly beyond the scope of this report.

Let us confine our discussion to examining the local response of a very simple structure consisting of a relatively thin metallic plate which forms the front face of a honeycomb sandwich structure. We assume that the front plate possesses no significant structural

strength or rigidity of its own but only a thickness of material, t_h, with finite density, ρ_h. We assume further that the honeycomb material is capable of exerting a constant resisting pressure as it is crushed. This constant-pressure assumption has been shown to be accurate and reliable over a very wide range of dynamic crushing situations if the crushing process is initiated before dynamic loads are applied via a precrush process.[13]

Let us start the analysis by evaluating the peak velocity imparted to the stagnation suface by debris cloud impingement. This evaluation is started by computing the mass per unit cross-sectional area of the plate. The specific local momentum transferred to the plate is then computed. This specific momentum is just the momentum per unit area contained within the debris cloud material as identified in the Equation 9 multiplied by a momentum multiplication factor, W, which can vary between W = 1 and 2. Arguments presented in Paragraph 2.5 indicate strongly that we may apply a momentum multiplication factor of W = 1 for impacts at supervelocities of optimum-size meteoroids.

We may now evaluate the instantaneous velocity imparted to the stagnation plate (on-axis), U_h, by supplying the cloud momentum per unit area (p_c from Equation 9) to the plate material and solving for plate velocity.

$$U_h = \frac{M_m U_m W (1 + G \sqrt{QK})^3}{4 \pi \rho_h t_h X^2 G^2 QK} \qquad (21)$$

The kinetic energy per unit area on cloud axis, e_h, associated with rearward motion of the stagnation plate may now be calculated as one-half the plate mass-per-unit-area times the instantaneous velocity squared as determined from Equation 21. The result is presented in Equation 22.

$$e_h = \frac{M_m^2 U_m^2 W^2 (1 + G\sqrt{QK})^6}{32 \pi^2 \rho_h t_h X^4 G^4 Q^2 K^2} \qquad (22)$$

This equation is of considerable interest for determining general factors associated with blast loading of underlying structures behind meteor bumpers. The most striking feature is that the energy per unit area imparted to the underlying structure drops with the fourth power of the separation distance, X, between the structure and the bumper. We may also note that the recoil energy per unit area of the stagnation plate is inversely propotional to its mass per unit area. The constant pressure required to crush honeycomb material allows peak deformation of the stagnated surface on-axis to be calculated very simply by noting that the energy per unit area of the stagnating plate is just equal to its out-of-plane displacement times the pressure resisting it. The result of applying this relationship to Equation 22 is presented in Equation 23 where the on-axis deformation, X, is related to all of the variables defined earlier plus the resisting pressure of the honeycomb material to crushing P_h.

$$\delta x = \frac{M_m^2 U_m^2 W^2 (1 + G\sqrt{QK})^6}{32 \pi^2 \rho_h t_h P_h X^4 G^4 Q^2 K^2} \qquad (23)$$

Let us complete this phase of the analysis by noting that the energy absorption capability of honeycomb material is proportional to honeycomb mass so that Equations 21 and 22 can be used to support shield weight optimization studies. Typical aluminum honeycomb has an energy absorption coefficient of 5×10^3 J/kg.

It is important to emphasize again that the arguments supporting Equations 22 and 23 are valid only in the limit that the stagnation surface has no bending strength or rigidity. All real structures have such strength and rigidity and, hence, are candidates for withstanding blows from debris clouds without a rear support.

Honeycomb structures are especially attractive for such service (in addition to their computational advantages) because their overall thickness-to-weight ratios are notably high which allows them to absorb relatively large bending impulse loads without collapsing. They also allow hard-point supports to be applied to their rear surfaces where they can be used safely to connect the panels to other structures since the maximum pressure that can be applied during a meteroid impact that is withstood successfully is the crushing strength of the honeycomb. Similar hard points exposed directly to oncoming debris clouds, as would occur if a simple stagnation plate is employed behind a bumper, are subjected to much more severe stresses associated directly with the stagnation process. A peak value for this pressure may be estimated by dividing the on-axis momentum per unit area of the front layer of the debris cloud by the time taken for front layer of the debris cloud to stagnate on the surface (cloud thickness as stagnation starts divided by peak cloud velocity, U_{max} of Equation 7). Expressions for cloud stagnating time, τ_c, and peak pressure on the stagnation surface P_{hd} are presented as Equations 24 and 25, respectively. (Note that Equation 24 is identical to Equation 11.)

$$\tau_e = \frac{X\ B\ G\ \sqrt{QK}\ (1 + KG^2)}{U_m\ (1 + G\ \sqrt{QK})^2} \qquad (24)$$

$$P_{hd} = \frac{W\ M_m\ U_m^2\ (1 + G\ \sqrt{QK})^5}{4\ \pi\ X^3\ G^3\ B\ (QK)^{3/2}\ (1 + KG^2)} \qquad (25)$$

Evaluating Equation 25 for the standard impact situation yields a value for the peak pressure on the front surface of the 2nd plate of P_{hd} = 146 MPA (21.5 ksi). The application time for this pressure (τ_c = 715 ns) for standard impact conditions is evaluated using

Equation 24. This time is short with respect to the time a shockwave would take to make a dual transit of a typical fastener. This situation may be expected to produce shock loadings. The application time, τ_c, is, however, longer than the dual transit time needed for similar waves to pass through typical face plates of honeycomb sandwich structures so we anticipate little or no shockwave-induced phenomena on these plates such as spallation, bond failure, etc.

2.7 RE-RADIATION FROM THE STAGNATION ZONE

The radiation output from the stagnated plasma behind a bumper impacted by a supervelocity meteoroid is enormously powerful. The peak intensity of this radiation on axis for the standard impact conditions exceeds 4×10^{12} W/m^2 (4×10^8 W/cm^2 and the area is several hundred square centimeters so that the total power output should exceed 10^{10} W. Another way of considering this situation is that radiation output from the stagnation zone probably encompasses the majority of the input kinetic energy from a large meteoroid striking the bumper (the energy output should approach 245 kJ for the standard impact conditions described in Table 2).

The process by which this radiation leaves the stagnation site is complicated considerably by the fact that the most energetic radiation produced is the result of material from the forward part of the debris plume impacting the stagnation plate near the axis. Radiation leaving the stagnation site is intercepted and at least partially absorbed by oncoming material from the rear of the debris cloud. This material is preheated before stagnation and may even start to radiate strongly before stagnating. This increased thermal energy before stagnation occurs, coupled with the lower approach velocity toward the stagnation site inherent in material near the rear of the debris bubble, should combine to reduce the peak power density (power per unit area) achieved during stagnation but to increase the overall energy release.

These arguments lead to the conclusion that the great majority of the kinetic energy of the original impact is expended in a

radiation pulse from an extended area of the stagnation plate. The energy of the photons radiated at maximum intensity is almost certainly below the peak photon energies computed using Equation 18 and the duration of the radiation pulse is near the time required for the entire debris bubble to stagnate (front and rear segments).

Ideally the radiation source would start as a small area on-axis when the debris bubble first contacts the stagnation plate and the diameter would then grow as the annulus of a circle until it reaches a maximum diameter near that of the oncoming debris cloud. The annulus radius would then shrink until a small homogeneous area of illumination terminates the radiation pulse as the last of the cloud stagnates. This ideal behavior is blurred substantially during the early and especially intense phases of radiation pulse because of the absorption and re-radiation of the emitted energy by rear elements of the debris cloud. The radiation pattern is expected to become progressively more ideal as the cloud stagnation continues since progressively less oncoming material is available to disrupt the process.

The radiation from a real cloud produced by a standard impact is certainly intense enough to heat severely all surfaces exposed to it at ranges up to several times the maximum diameter of the debris cloud. Should this heating occur in extremely short time periods, we might expect rapid thermal expansion of the surface material to produce shockwaves that could cause serious damage. The duration of the radiation pulse is long enough to assure that thermal shock loading is unlikely. We feel that structural responses to this radiation will be confined to surface vaporization, melting, and possibly scorching. Considerable amounts of secondary plasma can be produced by such processes which may create problems if it is confined to produce high pressures or is allowed to condense onto critical surfaces such as optical components, solar cells, electrical insulators, etc.

2.8 STRUCTURAL RESPONSE TO NON-IDEAL DEBRIS CLOUDS

The analyses presented so far in this chapter treat cases where all, or virtually all, of the debris cloud material is vaporous. We argued earlier in Paragraph 2.2 that the most common attacks of impact shields are expected to produce solid fragments in the debris launched behind the bumper plate and we identified the maximum size and velocity of these fragments. Potential exists that the meteoroid armor system can be defeated by these fragments perforating the second (stagnation) plate and damaging equipment behind it. Fortunately, both the maximum sizes and velocities of these fragments are well within regimes that can be investigated experimentally using conventional 2-stage light gas guns. A wealth of information is available concerning their damage potential when directed against a wide variety of targets as long as their spacial number density (total number per unit area) remains small enough to assure that synergistic effects caused by multiple particles striking at or near the same point remain unlikely.

We confine our consideration here to particles from an aluminum bumper striking a homogeneous hard aluminum stagnation plate. A variety of formulations are available for estimating the size and depth of the resulting craters and the ballistic limit thicknesses required for plate materials to avoid perforation. An analogous problem of determining the meteoroid size to produce a ballistic limit on the bumper has been analyzed in Paragraph 2.2 of this report. We propose to use the resulting formulation (Equation 2) for evaluating the crater dimensions produced by bumper particles. Again, the craters produced are hemispherical with their volumes proportional to the kinetic energies of the incoming particles. The proportionality constant, $R = 10^9$ J/m^3 is also usable for aluminum-on-aluminum impacts as well as silicate-on-aluminum ones. Applying Equation 2 to 1 mm diameter particles traveling at 5 km/s striking an aluminum backup plate (which is appropriate for the standard impact situation) produces the result that the radius of the crater, r_c, and its depth are approximately 1.62 mm. The

ballistic limit thickness for a hypervelocity impact into a homogeneous plate is near 1.5 times the depth of the crater produced by a similar impact into a thick block of the same material. Applying this criterion yields a ballistic limit thickness of d_{bl} = 2.42 mm as may be computed from Equation 26.

$$d_{bl} = \frac{3r_m}{2}\left(\frac{\rho_m U_m^2}{R}\right)^{1/3} \qquad (26)$$

2.9 COMMENTS ON THE OVERALL RELIABILITY OF THE ANALYSES

The extreme velocities of meteoroid impacts with space vehicles in general, and impacts associated with the Halley's Intercept Mission in particular, are well above those which can be achieved experimentally. As a result, considerable reliance must be placed upon: extrapolating experience gained at lower velocities to the meteoric velocity regime; developing impact mechanics theory; and conducting numerical experiments where detailed models of impact processes are exercised. The approach to the problem described in this chapter is the result of a combination of these techniques. We have applied results from detailed experiments conducted at velocities below 7.5 km/s to provide indications of rules governing impacts at meteoric velocities, but we have backed up these data with analyses of the physics expected to govern such processes. We have also made wide use of experimental data describing materials response to ultra-high pressure shockwaves produced by explosives and high velocity collisions. Finally, we have employed classical physics formulations for describing radiation output from materials at very high temperatures and densities.

The greatest extension of the phenomena controlling meteoric impact beyond experimentally reachable regimes occurs at the primary impact site where the incoming meteoroid is destroyed while bursting through the bumper. We feel that our qualitative understanding of shockwave motions through the impacted material is valid. On somewhat less firm ground are our assertions concerning the energy left behind in shocked material through entropy trapping. Our understanding of this process has been adequate to predict melting of aluminum and copper under laboratory impact conditions and also impact vaporization of cadmium, lead, and zinc.

A crucial assumption governing our analysis of meteoroid shield operation involves the impact vaporization of structural materials, such as hard aluminum alloys, by meteoric impact. Experimental verification of such vaporization is estimated to require impacts at minimum velocities of 12 km/s which are substantially above those that can be reached currently with macroparticle accelerators. An intense need exists to extend the state-of-the-art of laboratory ballistic technology to the point where either macroparticles can be launched reliably at velocities above 12 km/s or facilities for launching large microparticles can be instrumented to allow their use for observing impact vaporization processes quantitatively.

Relatively little is known about disassembly of solid materials under impact conditions to produce high velocity fragments. The proposed analysis of this process is sound as far as it goes, but we were forced to postulate maximum launched particle sizes far in excess of those which probably exist. Considerably more theoretical effort is required to examine the target breakup phenomena and this work should be backed up by experimental studies conducted within the hypervelocity regime reachable with current laboratory accelerators.

Finally, the assertion that the ratio of the masses per unit area of the bumper and incoming meteoroid is the only parameter controlling the efficiency of material disruption in the debris plume produced behind the impacted bumper is based strongly upon broad experimental evidence accumulated at velocities below 7.5 km/s. We

have not yet located sound theoretical arguments to justify accepting this rule as being applicable at meteoric velocities, but this rule appears to be vindicated at least approximately by checking against results of detailed computational considerations of meteoroids striking 2-layer armor.

The situation concerning analysis of debris plume expansion behind impacted bumpers is in a similar situation to that of the orignal impact process. We have available detailed experimental data concerning properties of debris plumes produced by impacts at and below 7.5 km/s. These data indicate strongly that the debris plume is a thin-walled shell which expands transversely as it proceeds rearward away from the impact site on the bumper. We have proposed a model for this process which is well grounded in conservation of linear momentum and energy, but which relies heavily upon the experimental observations that bumper material in the debris plume comes from the bumper directly under the impact site (or an area beyond known a priori) and that the debris plumes are relatively thin-walled shells. We also assume for computational convenience that the explosion producing the debris plume is a symmetrical one, i.e., that the mass per unit area and outward-directed velocity of material projected into the debris plume is independent of direction. These assumptions are adequate to explain at least qualitative features of actual impacts that occur at velocities achievable with laboratory accelerators. Experimental work is needed to verify that the model in its current form can predict data from laboratory experiments accurately. Further studies should be conducted to verify that the model is consistent with detailed computations of meteoric-velocity impacts.

The response of the debris cloud as it impinges upon the underlying structure to produce the cloud stagnation process probably rests on as firm a theoretical foundation as any phase of the process once the characteristics of the oncoming debris cloud are assumed. Our extensive argument about radiative energy transfer away from the stagnation zone is not complete since we have not developed

a quantitative model to describe absorption and reradiation of the radiation from the stagnation zone into the remainder of the oncoming cloud material. The final results of the process are relatively insensitive to this argument since they can have, at most, the effect of doubling impulse transmitted to the underlying structures. A better understanding of the process will almost surely change estimates of the impulse delivered by only a few percent.

Evaluating the response of the underlying structure after the impulse has been applied is inherently a complex problem which can be solved rigorously only through use of dynamic finite element analyses. We have simplified the structural specifications enormously in order to arrive at approximate solutions. In particular, we have chosen a honeycomb sandwich structure so that we can treat the energy absorption mechanism with relationships in closed form and we have made a relatively extreme assumption that the front plate possesses no lateral strength or rigidity. This strength/rigidity assumption is reasonably accurate when thin front plates supported by honeycomb are considered, but it is specifically invalid for treating thick plates. Our justification for presenting such an analysis is that it is reasonably easy to apply and it covers, at least approximately, many structures of current interest.

Finally, the entire analysis may be relied upon to deviate from reality in the conservative direction in all cases, i.e., the damage expected should be significantly less extreme than the predicted damage for any meteoroid impact of engineering interest.

The last matter considered in the analysis is the energy re-radiated from the stagnation zone. The existence of this radiation may be of extreme importance to the operation of space vehicles since a number of mechanisms are conceivable for coupling this energy into radiation sensors aboard the vehicle, thereby either destroying them or rendering their measurements inaccurate. This radiation may also be expected to produce plasma and vapor from the interior surfaces of the shield which can cause further mischief to the spacecraft. Our analysis of detailed interactions with the

radiation is currently at an early state of development and cannot yet be used to make reliable quantitative predictions and so no specific analysis is presented here.

Let us complete this discussion with some comments about potential for solving the entire problem through use of finite difference computational models. These computational models have been developed over the past two decades to the point where they are quite reliable for predicting many experimental results of importance for vehicle design (at velocities of 7.5 km/s and below). Unfortunately, these models are relatively awkward and expensive to use. This is particularly true for analysis of 2-layer meteoroid armor because many of the processes occur during extended periods so that the models have to be computed through many time iterations. Such processes are both slow and expensive, and produce substantial numerical difficulties because relatively low-level numerical instabilities are allowed time to grow to significance. Nevertheless properly executed finite difference numerical computations are probably the most reliable source of information currently available about the characteristics of meteoroid shield operation under realistic circumstances. The most effective use for these numerical analyses is to check specific results from less formal analyses such as the ones described here and finally to aid in verifying the safety of final shield designs.

3. METEOROID SHIELD DESIGN METHODOLOGIES

Our current understanding of the physics controlling the response of two-layer shields subjected to supervelocity meteoroid impacts is presented in Chapter 2. The next phase of the effort consists of developing methodologies for applying these principles efficiently to the design of effective meteoroid shields to protect space vehicles against specified meteoroid threats. We have chosen to address this task by: defining failure mechanisms for meteoroid shields; discussing in qualitative terms the characteristics of good meteoroid shield design; describing how meteoroid threat models are processed for application to shield design; and specifying the methods for optimizing a shield design to meet a specified threat using the physical models discussed in Chapter 2.

3.1 METEOROID SHIELD FAILURE MECHANISMS

Four separate mechanisms have been identified for causing meteoroid shields to fail. The first involves structural failure of the rear (stagnation) surface of the shield due to its receiving more impulse than it can dissipate without grievous damage. This mechanism assumes that either the transferred momentum intensity on-axis is great enough to cause failure of the underlying structure through local crushing, or that the total impulse from stagnating the entire debris cloud is too great to be withstood by the structure without gross failure. Localized crushing would occur when the underlying structure is a thin plate supported by honeycomb being crushed to its full extent, thus allowing residual impulse to be applied to the rear surface of the sandwich (at pressures greater than the crushing pressure of the honeycomb). This increase in loading intensity on the rear surface of the sandwich would cause it to deform grossly. Such deformation might: destroy equipment connected to the rear surface (which might also be launched rearward into the remainder of the vehicle's equipment); cause the rear plate to rupture and petal thereby allowing foreign material into the vehicle interior; or initiate cracks in the rear panel which lead to panel collapse during the current or a subsequent loading.

The second armor failure mechanism is produced by incoming meteoroids passing through holes in the bumper caused by previous impacts and striking the underlying surface directly. The resulting impacts may perforate the second surface or crater the second surface with material being projected behind it through spallation. Under either circumstance, debris is projected into the interior of the vehicle and perforation of the second plate renders the interior open to contamination from solid, liquid, and gaseous material produced by subsequent bumper impacts.

Honeycomb sandwich structures used as underlying elements behind meteoroid bumpers possess the obvious advantage that simple perforation of their front plates need not lead to serious vehicle damage since the rear surface of the honeycomb sandwich must be disrupted before catastrophe occurs. We have chosen in this analysis not to consider this eventuality in detail and to treat the possible use of the second plate of a sandwich as a "last-ditch" armor element. The resultant safety factor is used to account for unknowns remaining in our analyses. This approach may not be as conservative as it might seem because many vehicle designs rely heavily upon fastening critical equipment directly to the rear surface of a honeycomb sandwich underlying a meteoroid bumper. Sharp blows directed against the inside surface of such a panel could well damage equipment connected to it even though the plate itself remains intact.

The third failure mechanism involves the underlying structure being impacted by particles of bumper material launched during meteoric impacts where the incoming meteoroid is considerably smaller than the shield is designed to defeat. Since such meteoroids are relatively common compared to design-size ones, we anticipate that underlying structures are subjected to large numbers of impacts from solid bumper debris. The maximum size and velocity of such debris has been established for homogeneous metallic bumpers in Paragraph 2.8 of this report. It then becomes a relatively simple matter to establish the characteristics of the second (stagnation) surface of

the shield which can be expected to defeat them. The same comments regarding benefits of honeycomb sandwich structures for withstanding such impacts apply as were presented in the previous paragraph which considered direct meteoroid assault of the second surface.

The fourth failure mechanism involves a massive element such as a sensor or a fastener located at or near the plane of the bumper being struck directly by incoming meteoroids. Such an impact may be expected to break up the hard element and project relatively large chunks of debris rearward at considerable velocity against the underlying structure. The penetration capability of such chunks may be substantial and may produce failures of the meteoroid shield (and the entire vehicle) at meteoroid exposure levels well below those which would otherwise cause damage. Vehicle and shield designs involving such hard points should be avoided.

3.2 QUALITATIVE FEATURES OF EFFECTIVE METEOROID SHIELD DESIGNS

The first rule of effective meteoroid shield design is to minimize massive components made from dense strong material located at or near the bumper plane. A certain number of such elements are required for vehicle and meteoroid shield designs such as fastening/support points for the shield itself. We recommend that the total presented area of such points be minimized which reduces the probability of such areas being struck by large meteoroids. We suggest further that, where possible, these elements be fabricated from materials that produce minimally lethal fragments when impacted. A fine example of such material is carbon-fiber reinforced epoxy which is extremely strong and rigid, but which shatters virtually to powder upon hypervelocity impact.[14] Such material may be counted upon to produce impact debris of little or no consequence to the underlying structure.

The next most important rule is to choose a meteoroid bumper material which minimizes the lethality of solid particles that must inevitably be projected behind it. Let us start this discussion by considering the bumper material characteristics which should be

avoided. The worst bumpers would be made from dense rigid metal with a relatively high melting point such as tungsten, molybdenum, tantalum, titanium, nickel, iron, etc. The rigidity of these metals during shockwave loading effectively reduces the efficiency of shockwave heating through entropy trapping because entropy addition to material during shockwave transit decreases with increasing material rigidity. Thus, higher particle velocities are required to inject specific amounts of heat into the shocked material after it is returned to zero pressure. These higher particle velocities behind shockwaves of critical pressure levels lead to higher peak launch velocities for the resultant fragments. The metal should not be refractory because refractory materials characteristically have high fusion energies which, again, means that very high pressure shockwaves are required to melt them. Such waves produce high particle velocities, and again contribute to high peak velocities for projected solid fragments.

Finally, the material of the bumper fragments themselves is of importance because it controls their penetration effectiveness against underlying structures. Hypervelocity impact principles indicate strongly that penetration effectiveness of an impact is controlled by projectile velocity and density, and not material strength, but the velocity at which the hypervelocity approximations become valid increases markedly with the density and strength of the projectiles relative to the target materials.[15] The threshold velocity for these approximations is relatively close to the typical fragment projection velocities when underlying structures made from light structural materials (such as hard aluminum alloys) are considered. For instance, the threshold velocity for aluminum-on-aluminum impacts is generally considered to be between 2.5 km/s and 4 km/s (depending upon the alloy and heat treatment). Impact velocities between 5 km/s and 6 km/s are required to reach such thresholds when steel pellets are projected against aluminum targets. Considerably higher velocities are required to reach the hypervelocity regime when tungsten, tungsten carbide, and

tungsten-iron alloy projectiles are considered.

For this reason we recommend strongly that bumpers be made from materials with low densities and high shock compressibilities such as light soft metals, homogeneous plastics or plastic/fiber composites.

One specific class of bumper material bears special comment. If bumpers are fabricated from fiber-reinforced plastic, the sizes of bumper fragments which can be projected rearward is reduced sharply below those predicted for homogeneous metal bumper materials because the projected fragments break up into individual fibers and flakes of the binder component. In fact, the entire threat mechanism involving projected bumper fragments may be effectively eliminated. In addition, fibers in the bumper plate material adjacent to the impact site tend to expand laterally into the hole upon impact due to "fluffing" of the bumper material under action of the impact-induced shockwaves. The net effect of this fluffing is a significant reduction in the size of the open holes produced in bumpers by meteoroid exposure which, in turn, leads to significant reductions in the number (and hence maximum expected size) of undisturbed meteoric particles which may be expected to impact the underlying surfaces.

The next rule for good meteoroid shield design is to maximize the separation between the bumper and underlying structure. Maximizing this critical dimension provides the obvious advantage of reducing the intensity of blast loading caused by design-level impacts as can be seen by inspecting Equations 22, 23 and 25. Care must also be exercised to assure that bumper/underlying structure spacing is adequate to assure that individual particles of bumper material are spaced far enough apart to prevent synergistic effects which might otherwise occur when individual impact craters on the underlying surface are close together. The most extreme example of such effects is the impact of two particles at the same point where the second one strikes in the crater floor produced by the first and, therefore, "sees" a thinner material layer to perforate or spall. In most cases, this particulate impact limitation upon spacing between bumpers and underlying structures is much less severe than the

blast-loading criterion and is, therefore, met automatically.

The final rule for effective shield design is to maximize the blast loading and particle perforation strength of the underlying structure. Special care must be taken to assure that secondary damage mechanisms such as shock propagation through the underlying structure to equipment behind are accounted for properly in overall shield/vehicle designs. This exercise may vary from straightforward to requiring its own research effort depending upon the individual situation.

3.3 EVALUATING/PROCESSING METEOROID THREAT MODELS

Clearly the first and one of the most important steps for designing meteoroid protection for a space vehicle is to establish the meteoroid impact threat to which the vehicle is subjected. This threat is a function of the vehicle size, the duration of exposure, and the anticipated meteoroid fluxes through which it must fly. The threat is generally expressed in terms of the number of meteoroids within a specified size (mass) range that are intercepted, per unit of presented vehicle area, per unit of time.

A cometary intercept mission such as the Halley's Intercept Mission has a number of special features from a meteoroid impact viewpoint. First, the critical flux levels are concentrated in a volume surrounding the comet itself so that the critical meteoroid environment is experienced by the encountering vehicle for only a small fraction of its time in space rather than the entire duration of the flight. Second, the velocity vector of all the critical meteoroid material with respect to the vehicle is known with some precision so that their direction of approach relative to the vehicle axis can be established as can be the angle upon which they engage the shield (generally normal angle).

Considerable effort has gone into establishing the expected meteoroid threat levels for a wide variety of near-Earth and deep-space missions. Many of these threat models are now based, at least in part, upon experimentally-gathered data as well as results of theoretical predictions. The threat models of greatest interest

to the current effort have been developed through detailed consideration of the meteoroid veil surrounding Halley's comet shortly after it undergoes perihelion (during the early Spring of 1986). The most up-to-date model [1] has been computer analyzed by Dr. Neil Divine of JPL who maintains a program capable of predicting meteoroid flux and fluence levels vs. meteoroid size (mass) for vehicles traveling along prescribed trajectories which carry them near Halley's Comet.[2] His current model assumes that material is ejected from the comet symmetrically but is then acted upon by solar wind and radiation pressure. The vehicle trajectory relative to the comet may be specified simply by stating the solar trajectory angle, the encounter date, and the distance of closest approach to the comet. The model output is a listing of meteoroid fluxes (in terms of meteoroid size vs. number of impacts per unit area per unit time) and mission fluences (number of meteoroids per unit area per mission). The fluence listings describe the total number of impacts from meteoroids in a continuous sequence of given size ranges against a unit presented area of the vehicle during its traverse of the entire cometary veil. Meteoroid fluences have also been calculated with this program for one-half of the mission (until the vehicle reaches its closest point to the comet) for analyzing hazards of missions like the European Space Agency's Giotto project where the vehicle is expected to remain useful only until it passes the comet.

Typical outputs from Dr. Divine's program are presented in Figure 7 and a plot of this data directly usable for meteoroid shield design is presented in Figure 8. Not presented explicitly in Dr. Divine's printed outputs is the estimated uncertainty of the model. This uncertainty level is quite large (+ 1σ of uncertainty in fluence levels exceeds a factor of 2 under most circumstances). The + 1σ value associated with the data presented is plotted in Figure 8.

PARTICLE THRESHOLD		RELATIVE SPEED (m/s)	INTERVAL FLUENCE				
MASS (kg)	RADIUS (m)		NUMBER (m^{-2})	AREA –	MASS (kg/m^2)	MOMENTUM (kg/sm)	ENERGY (J/m^2)
3.58-17	1.21-07	6.02+04	3.41+05	2.52-08	1.97-11	1.18-06	3.56-02
6.50-17	1.63-07	6.02+04	1.93+06	2.07-07	1.64-10	9.84-06	2.96-01
1.00-16	2.00-07	6.02+04	5.14+07	2.49-05	2.31-08	1.39-03	4.19+01
1.00-15	5.47-07	6.02+04	4.74+07	1.12-04	1.53-07	9.22-03	2.77+02
1.00-14	1.32-06	6.02+04	1.37+07	1.58-04	3.81-07	2.29-02	6.89+02
1.00-13	3.00-06	6.02+04	2.23+06	1.21-04	5.75-07	3.46-02	1.04+03
1.00-12	6.59-06	6.02+04	2.84+05	7.25-05	7.18-07	4.32-02	1.30+03
1.00-11	1.43-05	6.02+04	3.54+04	4.24-05	8.93-07	5.37-02	1.62+03
1.00-10	3.09-05	6.02+04	4.52+03	2.52-05	1.14-06	6.86-02	2.06+03
1.00-09	6.68-05	6.02+04	5.91+02	1.53-05	1.49-06	8.96-02	2.70+03
1.00-08	1.44-04	6.02+04	7.92+01	9.55-06	2.00-06	1.20-01	3.62+03
1.00-07	3.10-04	6.02+04	1.09+01	6.09-06	2.74-06	1.65-01	4.97+03
1.00-06	6.68-04	6.02+04	1.53+00	3.99-06	3.87-06	2.33-01	7.01+03
1.00-05	1.44-03	6.02+04	2.25-01	2.72-06	5.68-06	3.42-01	1.03+04
1.00-04	3.10-03	6.02+04	3.53-02	1.97-06	8.89-06	5.35-01	1.61+04
1.00-03	6.68-03	6.02+04	6.27-03	1.63-06	1.58-05	9.51-01	2.86+04
1.00-02	1.44-02	6.02+04	1.59-03	1.92-06	4.01-05	2.41+00	7.26+04
1.00-01	3.10-02	0.00	0.00	0.00	0.00	0.00	0.00
1.00+00	6.68-02	0.00	0.00	0.00	0.00	0.00	0.00
GAS MOLECULES →			1.15+20	1.11+01	4.28-06	2.57-01	7.73+03

Figure 7. Tabulation of Cometary Meteoroid Fluences for Halley's Comet Encounter Mission on 26 March 1986 With a Minimum Approach Distance of 800 KM as Predicted by the JPL Cometary Dust Model. (Reference 2)

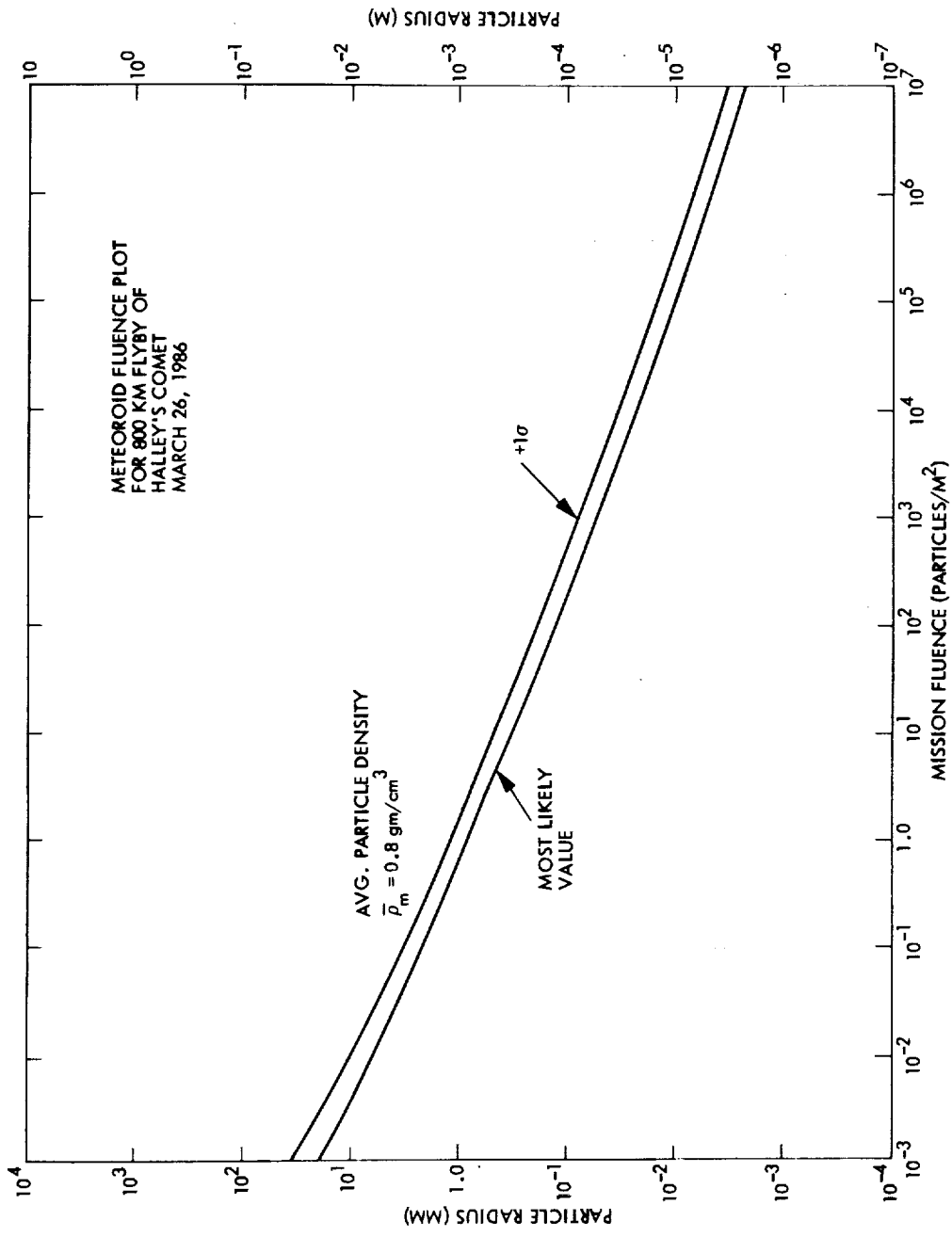

Figure 8. Graphic Plot of Meteoroid Fluence vs. Meteoroid Size for a Complete Halley's Comet Encounter Mission on 26 March 1986 With a Minimum Approach Distance of 800 KM as Predicted by the JPL Meteoroid Dust Model (Reference 2) The Lower Curve Represents Model Predictions; the Upper Curve Represents One Standard Deviation Above the Estimates.

Note that the number of particles per square meter of presented area per mission in the printout ranges from thousands for small particles to small fractions of unity for the larger particles. Multiplying these numbers by the area of the bumper shield provides estimates of the total number of particles in the size range considered striking the shield. When these values are significantly less than unity, they may be interpreted as impact probabilities, i.e., a fluence of 10^{-4} particles per vehicle area infers a probability of 0.01% of the vehicle receiving an impact from a meteoroid in the specified size range.

Specialized calculations are carried out by assuming other areas besides the entire area of the vehicle. For instance, the probability of a hard point at or near the bumper plane being impacted is equal to the fluence for the particle size of interest times the total area of all exposed hard points.

In general the entire range of meteoroid sizes evaluated is not of interest to any particular threat calculation. The smallest particle of interest for a 2-element meteoroid shield computation is generally the particle that can just perforate the bumper. The interest range is usually truncated at the upper meteoroid size limit by the maximum meteoroid size which is to be protected against.

3.4 QUANTITATIVE TECHNIQUES FOR OPTIMIZING EFFECTIVE METEOROID SHIELD DESIGNS

The basic design methodology for specifying an optimized meteoroid shield involves: assuring that the chance of failure due to each threat does not exceed the vehicle failure probability budget alloted to shield failure from that threat; and balancing the strength of the shield against specific threats so that no excess shield capability is provided to resist one threat at the expense of either total vehicle mass or shield strength to resist one of the other threats. As specified in Paragraph 3.2, the threats to be considered are: blast loading of the second structure from a debris cloud produced by a design-size meteoroid; impact of the second structure by meteoroids passing through holes in the bumper; impact

of the underlying structure from bumper debris produced by impacts from relatively small meteoroids; and impact of the underlying structure by debris from meteoric impacts of hard points at or near the bumper plane. We do not consider danger from hard point impacts near the bumper further since such an analysis depends strongly upon details of the individual hard points (particularly upon how they break up under hypervelocity impact). We assume here that hard points either do not exist or that they produce no lethal fragments upon impact.

The following is a summarization of steps required for conducting the design optimization.

1. Evaluate the largest meteoroid whose probability for impacting the vehicle is great enough to consider.
2. Evaluate bumper parameters needed to provide optimum disruption of the particle evaluated in Step 1.
3. Evaluate the maximum size and velocity of bumper debris created by impacts of relatively small meteoroids.
4. Evaluate minimum impact resistance paramaters of underlying structure needed to withstand bumper fragments.
5. Evaluate smallest meteoroid that can perforate the bumper.
6. Evaluate total surface area of the bumper opened by perforating impacts.
7. Evaluate maximum meteoroid size/mass which can pass through holes in the bumper and strike the underlying surface (designated by step 4) directly without causing it to fail.
8. Evaluate the shield failure probability caused by a particle determined in Step 7 striking the underlying structure.
9. Evaluate structural parameters that can just survive blast loading from a maximum design meteoroid impact of the bumper.

10. Choose largest feasible bumper spacing (if any) and derive the mass-per-unit area of honeycomb core material needed to assure shield survival.
11. Select a candidate underlying structure (such as a honeycomb sandwich) whose front plate can just withstand the particle impact threats designated in step 4 without perforation. Evaluate bumper/structure spacing which just allows the structure to survive the blast loading.
12. Evaluate total probability of shield failure. Compare the probability of failure due to the two basic threats (Step 1 and Step 8) to the budget. The third and fourth threats (from debris of first surface and hard points) are zero by definition for this analysis.

The remainder of this chapter is a discussion of each of these 12 steps with suggestions about how they should be accomplished.

3.4.1 Identify Largest Meteoroid

The first step in identifying the largest meteoroid to be considered is to decide upon the maximum acceptable probability of an impact that causes vehicle destruction. The procedure for choosing this probability involves an overall hazard analysis for the vehicle conducting its mission and philisophical determination of the maximum acceptable mission failure probability. American practice is to establish such information via systems studies and assign the shield designers a failure probability budget. Once the failure probability has been chosen, a portion of it is budgeted to failure mode 1 (blast loading of underlying structure). It is divided by the presented area of the vehicle to determine the equivalent meteoroid cumulative fluence to produce such an impact probability. This fluence level is then looked up on a graphic plot of meteoroid size vs. fluence (such as Figure 8) to identify the equivalent meteoroid size (mass).

3.4.2 Evaluate Meteoroid Bumper Parameters

The mass per unit area of the bumper required to provide optimum pulverization of the maximum design meteoroid is calculated as having one-quarter the mass per unit area of the maximum design meteoroid. Choice of a material for the bumper (and its density) may then be used to specify the bumper material thickness. (Note that choice of bumper material affects vulnerability of the underlying structure to bumper fragments.)

3.4.3 Evaluate Maximum Size and Velocity of Bumper Debris

The maximum size of bumper debris considered is a sphere whose diameter equals the bumper thickness according to our model described in Paragraph 2.8 of this report. The maximum velocity of the bumper material is dependent upon the shock compressibility of the material and its fusion energy. The maximum velocities for solid particles projected behind bumpers made from typical materials of current interest are evaluated in Table 2 and techniques for establishing such values for numerous other materials whose shock and thermal physics data is available is presented in Reference 10.

3.4.4 Evaluate Protection Required to Resist Bumper Fragments

Bumper fragments are simply pellets traveling at conventional hypervelocities (3 km/s to 7km/s) whose impact cratering efficiencies are either available in the literature or are established readily. Effective meteoroid bumper designs employ materials of low density and relatively low mechanical strength which assure that impacts between their maximum-lethality fragments and the materials of the underlying structures obey hypervelocity approximations. The ballistic limit thickness of underlying surfaces to just withstand such impacts may be evaluated using Equation 26. Care should be taken, however, to assure that the impacts are, indeed, in the hypervelocity regime. Should they prove not to be, principles outlined in Reference 15 should be applied for estimating penetrating

effectiveness of meteoroid debris.

3.4.5 Evaluate Size of Smallest Meteoroid That Can Perforate Bumper

All impacts between meteoroids and structural materials are well within the hypervelocity regime. The sizes and shapes of the resulting craters can be predicted with reasonable accuracy using simple cratering formulations such as the one presented in Equation 2. The ratio of meteoroid diameter to ballistic limit thickness is approximately 1.5 times the ratio of the radius of a crater (crater depth) from an equivalent impact into a thick plate of bumper material to projectile radius as evaluated in Equation 2. The ballistic limit criterion is presented in Equation 26. This equation may be used along with the predetermined impact velocity to calculate the minimum meteoroid diameter which will just perforate the bumper whose thickness and material have already been specified to provide optimum disruption of the largest design meteoroid using procedures described in Paragraph 3.4.2.

3.4.6 Evaluate Maximum Surface Opened in Bumper Plate by All Impacting Meteoroids

Our method for estimating hole sizes produced in bumpers by impacting meteoroids is described in Section 2.3. We choose the conservative approach to estimating hole sizes that involves each meteoroid capable of perforating the bumper producing a crater whose radius is described by Equation 2, i.e., a hole whose size equals that of a crater that would have been produced by the meteoroid impacting a thick block of bumper material. This assumption is followed as progressively larger meteoroids are considered until the maximum hole diameter criterion is met (as shown graphically in Figure 2). The hole sizes in the bumper relative to meteoroid sizes are then evaluated by a linear decreasing function in the left-hand portion of Figure 2 until the design-size meteoroid is reached.

The steps required for evaluating the total hole area starting

with holes produced by the smallest meteoroids above the ballistic limit size are presented below.

A. The ratio of meteoroid diameter to maximum hole diameter is calculated using Equation 2.

B. The number of meteoroids in the size range immediately above the ballistic limit size is calculated by multiplying the expected number per unit area as read from a listing of the meteoroid threat (such as the one presented in Figure 7) by the shield area. The total number of impacts is then multiplied by the area of each resulting hole calculated from the hole size established in Paragraph 3.4.1, (Step 1).

C. The procedure in Step B is continued for each size range listing in the meteoroid threat table until the meteoroid size producing the maximum hole diameter is reached.

D. The process is contined beyond maximum hole size until the design size is reached but the value for the hole size is read from the graphical presentation in Figure 2 rather than through use of Equation 2. Note that a point is inevitably reached in Step 3 or 4 where the number of impacts expected over the vehicle bumper falls to below unity. The procedure may be continued through this limit without change but the interpretation of the number of impacts becomes a probability that an individual impact will occur during the duration of the mission.

E. All of these hole areas for individual meteoroid sizes are added to determine the total area of the bumper opened by impact which allow meteoroids to impinge upon the underlying structure directly.

3.4.7 Evaluate Meteoroid Size Which Just Fails The Underlying Structure When Impinging Upon It Directly

Equation 26 may now be used with meteoroid impact velocity, and the cratering efficiency parameter, R, to calculate the ballistic limit meteoroid size of the surface plate on the underlying structure sized in Paragraph 3.4.4.

3.4.8 Evaluate Chance of Failure to Underlying Plate Caused by Direct Impingement

Before continuing let us consider characteristics of the bumper perforation process. This process begins as soon as the vehicle is exposed to the threat and continues until threat exposure is terminated. If the threat intensity is constant, or at least is nearly a symmetrical function with respect to some critical time (such as the closest approach to a comet during an encounter mission), we may assume that the area of the bumper open for meteoroid transit increases proportionally to application of the threat. Thus, we may assume for calculation that only half of the open area evaluated in Paragraph 3.4.6 (Step 6) is available to the full meteoroid threat.

We take this revised area, A, (half of that calculated using procedures described in Paragraph 3.4.6) and multiply it by the cumulative fluence, F, of meteoroids larger than the size evaluated in Pargraph 3.4.7 (Step 7) to obtain the probability of such a meteoroid failing the structure. Actually one minus the probability, P, is the base of natural logarithm raised to the negative power of the product as presented in Equation 27.

$$1 - p = \exp(-AF) \qquad (27)$$

The effect of the hole edges breaking up particles may be included more accurately by performing a double integration to

perform the function of this paragraph and conducting the operations specified in Step 6 (Paragraph 3.4.6) simultaneously.

3.4.9 Blast Loading of Underlying Structure

We may now turn our attention to evaluating the response of the underlying structure to blast loads. Clearly the most devastating blast loads to underlying structures is produced by a design-sized meteoroid striking the bumper. The energy intensity transferred to the front plate of an underlying structure from such an impact may be evaluated using Equation 22. If we assume the underlying structure is a honeycomb sandwich, we may develop an expression for the weight of core which will just lead to complete honeycomb crushing when the thickness of the front plate has been chosen to just defeat bumper particles evaluated in Paragraph 3.4.3 (Step 3) and directly impinging meteoroids of maximum lethality. This expression is derived by evaluating the energy required to crush honeycomb using Equation 28 where e_{cr} is the energy per unit area required to completely crush honeycomb.

$$e_{cr} = C \rho_c t_c \tag{28}$$

The term, C, is the energy per unit mass that can be absorbed by the honeycomb through crushing and ρ_c and t_c are the density and thickness of the honeycomb core respectively.

Equating e_{cr} with the energy imparted to a unit area of the honeycomb facing plate on axis, e_h from Equation 22 with the maximum practical bumper spacing, X, and solving the resulting equation for the mass of the critical meteoroid that just produces honeycomb sandwich structure failure produced Equation 29. The maximum practical spacing, X, may be constrained by geometry or as a multiple of an incoming particle diameter.

$$M_m = \frac{4 \pi X^2 G^2 QK \sqrt{2 C\rho_h t_h \rho_c t_c}}{U_m W (1 + G \sqrt{QK})^3} \qquad (29)$$

Equation 29 defines the minimum $\rho_c t_c$ of the underlying sandwich structure to survive a design limit impact. Note that the mass per unit area of the honeycomb core and not its thickness is specified in this analysis. The absolute thickness of the honeycomb is, obviously, inversely proportional to honeycomb density. In general, the ability of the honeycomb sandwich panel to withstand the total impulse of a design meteor blow is increased as the thickness of the honeycomb sandwich is increased (through use of low density honeycomb core material) due to the increased structural rigidity produced by increasing separation of the front and rear plates. The overall space taken up by the panel also increases, however, which may be limited by vehicle design considerations. The honeycomb material also tends to lose its efficiency, C, for absorbing energy through crushing as its density is reduced to low values (see Reference 13).

The third surface (rear surface of the honeycomb sandwich) of the shield is designed to transmit the local loading to the shield support points. Since momentum is conserved and the shield is much heavier than the particle, the shield momentum is given by Equation 30

$$M_s U_s = M_m U_m \qquad (30)$$

where: U_s and M_s are the local recoil velocity of the shield and the shield mass participating in the reaction.

Evaluation of M_s is not straightforward since it depends upon the configuration of both the honeycomb sandwich structure and its supports. An approximation valid for many typical structures is that

M_s is the mass of a circular portion of the structure centered on the support and extending to the nearest shield edge.

The kinetic energy of the shield, e_k is:

$$e_k = \frac{1}{2}\left(M_s\ U_s^2\right) \tag{31}$$

Substituting Equation 30 into 31, we get:

$$e_k = (M_m\ U_m)^2 \ /\ 2M_s \tag{32}$$

The first inclination is to equate e_k to the elastic energy absorption capability of the structure. Inelastic deformation is a much more effective energy absorption mechanism! It may be better to allow the support points to crush into the sandwich to absorb shield kinetic energy just as crushing under the front surface absorbs cloud energy.

For the potentially most troublesome case (of an impact directly opposite a support), three failure mechanisms have been identified: 1) excessive core crushing stroke; 2) panel bending failure around the support; and 3) core shear failure around the support circumference. The first failure mechanism (excessive core stroke) occurs when the kinetic energy of the local shield, e_k, exceeds the energy absorption capability of the honeycomb material opposite the support foot. This mode is defeated by assuring that the foot of the support has sufficient area to engage enough honeycomb core to assure complete energy absorption via crushing. The second (bending) failure mode is defeated by assuring that the bending strength of the panel is adequate to transfer the induced inertial loads to the support without failure. The third mechanism (core shear failure) is defeated by making the core shear strength evaluated at the perimeter

of the support foot greater than the reaction force (core crushing strength times the support foot area).

Impacts between supports can also trigger shield failure due to bending of the honeycomb panel. The worst-case situation occurs when a design level impact occurs midway between supports. The support reaction forces used to analyze this failure mode are those calculated for an impact opposite a support.

3.4.10 Largest Practical Bumper Spacing

Spacing between the bumper and the underlying structure affects strongly the blast resistance of the underlying structure but is usually fixed by vehicle design considerations. It may also be constrained to a multiple of the design partical diameter.

3.4.11 Total Probability of Failure

The probabilities of failure evaluated in: 3.4.1, blast load from design-size impact; and 3.4.8, impact of second surface by meteoroid passing through a bumper hole; should be combined and compared to the failure probability budget for the vehicle shield. Note that the probabilities of failure due to first surface and hard point debris are zero by design. Should significant differences between the budget and the total failure probability exist, the shield design must be iterated systematically to arrive at an optimized shield design.

The optimization should be conducted iteratively using two relations. The first is the constraint condition that the combined probability of failure from all threats must not exceed the prescribed failure budget. The second relation is that the total weight of the protective system should be minimized.

The procedure proposed for carrying out the optimization process involves scaling the critical shield dimensions for the trial design that were developed using procedures described in Paragraphs 3.4.1 to 3.4.10. The critical shield dimensions: t_b (bumper thickness); t_h (thickness of the front face); t_c (honeycomb core thickness); t_3 (rear surface thickness of the honeycomb panel; and X (bumper-panel

spacing) are scaled to their optimized values, t_{bo}, t_{ho}, t_{co}, t_{3o} and X_o respectively.

We start the optimization by defining three critical meteoroid sizes associated with failure of the shield: (1) design meteoroid; (2) smallest meteoroid that can perforate the bumper; (3) and the smallest meteoroid that can perforate the front surface of the sandwich panel (t_2). We identify the local slopes of the cumulative meteoroid mass fluence curves at these points as: β_m, β_b, β_2 respectively.

Let us identify a new variable, ξ, to reflect the possibility that the optimized second surface thickness may be greater than that of the scaled trial design which was specified to provide protection against bumper debris.

$$\xi = \frac{t_{bo}}{t_b} \frac{t_h}{t_{ho}} \tag{33}$$

Note that $\xi = 1$ under all circumstances.

Two cases for optimization have been identified depending upon whether the bumper-sandwich spacing, X, is constrained by vehicle design envelope considerations or as a multiple of design meteoroid size (as discussed in Paragraph 3.4.10).

The product of the cumulative fluence of meteoroids larger than these critical values and the appropriate target area is the number of particles that will produce shield failure. These will be designated as N_m and N_b for the blast threat and the direct penetration of the front face of the sandwich through holes in the bumper respectively. Note that the shield failure probabilities associated with each of these threats are: $1 - P_m = \exp(-N_m)$; and $1 - P_h = \exp(-N_2)$ which are nearly N_m and N_h respectively when these values are much less than unity. The sum of $N_t = N_m + N_b$ is related to the total probability of shield failure, P_t by:

$$N_t = -\ln (1 - P_t) \qquad (33A)$$

Equation 33A is expressed in terms of N_t to reflect the fact that a bound on P_t is a given system constraint. The value used in subsequent analyses is always the value required to assure adequate vehicle mission reliability.

The value N_m is associated with the largest meteoroid protected against which was evaluated in Paragraph 3.4.1 for the trial design. The trial design thickness of the front surface of the second plate, t_2, is scaled by t_{20}/t_2. We can evaluate N_{mo} by Equation 34 based on K = 0.25.

$$N_{mo} = N_m \left(\xi \frac{t_{ho}}{t_h} \right)^{3\beta_m} \qquad (34)$$

The exponent $3\beta_m$ reflects the change in the number of damaging particles since M_m is proportional to t_b^3.

The value of N_{h0} is associated with direct perforation of the second surface by particles passing through holes in the bumper. The fluence of damaging particles can be scaled as was done for N_{mo} except $3\beta_h$ is used since the mass of the meteoroid that will just perforate the second surface, M_m is proportional to t_h^3. The applicable area must also be scaled by $(t_{h0}/t)^{2 + 3\beta_b}$. The $3\beta_b$ is the exponent needed to reflect the change in the number of particles that can perforate the scaled bumper thickness since M_m is proportional to t_b^3. The 2 reflects the change in the size of each hole under the assumption that bumper hole diameters are linearly related to impacting meteoroids diameters. The term, N_{h0} can be evaluated by Equation 35 which combines these effects.

$$N_{ho} = N_h \left(\xi \frac{t_{ho}}{t_h} \right)^{2+3\beta_b} \left(\frac{t_{ho}}{t_h} \right)^{3\beta_h} \quad (35)$$

The overall constraint condition on success probability can be written as shown in Equation 36 using these values of N_{mo} and N_{h0} which are used to define a Lagrangian boundary constraint.

$$H \equiv N_{mo} + N_{ho} - N_t \quad (36)$$

$$H\left(\frac{t_{ho}}{t_h} , \xi \right) = 0 \quad (37)$$

The protection system weight can also be scaled from the trial design. The first surface weight is scaled by $(\xi t_{h0}/t_h)$ and the second surface weight by (t_{h0}/t_h):

$$W_{bo} = W_b \, \xi \left(\frac{t_{ho}}{t_h} \right) \quad (38)$$

$$W_{ho} = W_h \left(\frac{t_{ho}}{t_h} \right) \quad (39)$$

where the W's refer to weights of the components designated by the subscript convention that b refers to the bumper and h refers to

the front face of the honeycomb sandwich structure. Note that the W's are proportional to their associated t's.

The core weight, W_c, can be scaled similarly by $M_m^2/X^4 t_{h0}$ from the trial core design calculated using Equation (22).

$$W_{co} = W_c \left(\frac{M_{mo}}{M_m}\right)^2 \left(\frac{X}{X_o}\right)^4 \left(\frac{t_h}{t_{ho}}\right)$$
$$= W_c \, \xi^6 \left(\frac{t_{ho}}{t_h}\right)^5 \left(\frac{X}{X_o}\right)^4 \qquad (40)$$

since M_m is proportional to t^3_{bo}.

The third surface weight, (rear face of the honeycomb sandwich) W_3, can be scaled by $M^2_m/M_s t^2_{co}$ for a given configuration as derived in Paragraph 3.4.10. In order to simplify this expression, assume $M_s = \eta t_{h0}$ because most of the shield mass is concentrated in the honeycomb sandwich and the other components roughly scale with it. The term, η, is nearly constant for small changes in design.

$$W_{30} = W_3 \, \xi^{-6} \left(\frac{t_{ho}}{t_h}\right)^{-5} \frac{\eta}{\eta_o} \left(\frac{X_o}{X}\right)^8 \qquad (41)$$

The total shield weight is given by Equation 42.

$$W_t \equiv W_b + W_h + W_3 + W_c \qquad (42)$$

The total protection weight can be minimized with the Lagrangian boundary constraint H = 0 using a Lagrangian multiplier (λ) by setting the partial derivitives of $J(t_{h0}/t_h \xi)$ with respect to

(t_{h0}/t_h) and ξ equal to zero where J is defined by Equation 43.

$$J\left(\frac{t_{ho}}{t_h}, \xi\right) \equiv W_t - \lambda H\left(\frac{t_{ho}}{t_h}, \xi\right) \tag{43}$$

Two cases must be considered. The first assumes the idealized bumper-sandwich spacing, X_o, is a constant due to vehicle design limitations. The second assumes X_o to be proportional to the limiting meteoroid diameter for perforating the front sandwich face and $X_o = X\ (t_{h0}/t_h)$. The function, J, is evaluated for each case. It is differentiated with respect to the two variables, t_{h0}/t_h and ξ in turn and each derivitive is set equal to zero. The resulting equations are solved for the Lagrangian multiplier, λ, and the results are subtracted from one another and set equal to $L(\lambda)$.

$L(\lambda)$ must obviously equal zero. The value for, ξ, which satisfies this relationship is extracted numerically. This value for, ξ, is the one required to compute optimum values for all the shield parameters.

Case 1

X. at configuration limit: $X = X_o$

$$J \cong \left(\frac{t_{ho}}{t_h}\right)(\xi W_b + W_h) + \xi^6\left(\frac{t_{ho}}{t_h}\right)^5 W_c + \xi^{-6}\left(\frac{t_{ho}}{t_h}\right)^{-5}\left(\frac{\eta}{\eta_o}\right) W_3 - \lambda(H) \tag{44}$$

$$\left(\frac{t_{ho}}{t_h}\right)\frac{\partial J}{\partial\left(\frac{t_{ho}}{t_h}\right)} = W_{bo} + W_{ho} + \left(5W_{co} - 5W_{30}\right)\xi - \lambda\left\{3\beta_m N_{mo} + (2 + 3\beta_{bo} + 3\beta_{ho}) N_{ho}\right\} = 0 \tag{45}$$

$$\xi \frac{\partial J}{\partial \xi} = W_b + G\,(W_{co} - W_{30}) - \lambda \left\{ 3\beta_{mo}\, N_{mo} + (2 + 3\beta_{mo})\, N_{ho} \right\} = 0 \quad (46)$$

Solve the last two equations for λ and identify the difference as $L(\lambda)$.

$$L(\xi) \equiv (W_{bo} + W_{ho} + 5W_{co} - 5W_{30}) \Big/ \left\{ 3\beta_{mo}\, N_{mo} + (2 + 3\beta_{mo} + 3\beta_{ho})\, N_{ho} \right\} - (W_{bo} + 6W_{co} - 6W_{30}) \Big/ \left\{ 3\beta_{mo}\, N_{mo} + (2 + 3\beta_{mo})\, N_{ho} \right\} = 0 \quad (47)$$

The value for ξ satisfying this expression is extracted numerically.

Case 2

X_o proportional to d_m, $X_o = X\, t_{h0}/t_h$)

$$J \approx \left(\frac{t_{ho}}{t_h}\right)(\xi\, W_b + W_h) + \xi^2 \left(\frac{t_{ho}}{t_h}\right) W_c + \xi^2 \left(\frac{t_{ho}}{t_h}\right)^3 \left(\frac{\eta}{\eta_o}\right) W_3 - \lambda(H) \quad (48)$$

$$\left(\frac{t_{ho}}{t_h}\right) \frac{\partial J}{\partial \left(\frac{t_{ho}}{t_h}\right)} = W_{bo} + W_{ho} + W_{co} + 3W_{30} - \lambda \left\{ 3\beta_{mo}\, N_{mo} + (2 + 3\beta_{mo} + 3\beta_{ho})\, N_{ho} \right\} = 0 \quad (49)$$

$$\xi \frac{\partial J}{\partial \xi} = W_{bo} + 2W_{co} + 2W_{30} - \lambda \left\{ 3\beta_{mo} X_{mo} + (2 + 3\beta_{mo}) N_{ho} \right\} = 0 \quad (50)$$

Solve the last two equations for λ and identify the difference as $L(\lambda)$.

$$L(\xi) = (W_{bo} + W_{ho} + W_{co} + 3W_{30}) \Big/ \left\{ 3\beta_{mo} N_{mo} + (2 + 3\beta_{mo} + 3\beta_{ho}) N_{ho} \right\} \quad (51)$$

$$- (W_{bo} + 2W_{co} + 2W_{30}) \Big/ \left\{ 3\beta_{mo} N_{mo} + (2 + 3\beta_{mo}) N_{ho} \right\} = 0$$

The value for ξ satisfying this expression is extracted numerically.

In either case the value of λ which satisfied $L(\lambda) = 0$ is found using the trial values of W_b and W_h. Then the value of t_{h0}/t_h which satisfies $H(t_{h0}/t_h, \xi) = 0$ is found using the previously calculated value of ξ. The last two processes can be repeated until there is negligible change. The two processes can be carried out separately since the first corresponds to finding the optimum ξ for an undetermined failure probability, P_f, and the second corresponds to satisfying H for a non-optimum ξ. The process can be started with either equation. The values leading to optimized W's and N's should be found at each step. If desired, the t_h/t_b, can be plotted as a function of ξ for both H and L. Crossing of the two curves represents a solution of both equations.

When evaluating W_e the approximation using ξ should not be used.

Instead;

$$W_{30} = W_3 \left(\frac{t_{ho}\xi}{t_h}\right)^6 \Big/ \frac{W_{To}}{W_T}\left(\frac{W_{co}}{W_c}\right)^2 \qquad (52)$$

Equation 52 assumes the use of the minimum acceptable core density., i.e. t_{co}, is not limited.

Equation 52 can be solved for W_3 even though W_t includes W_3:

$$W_{30} = -(W_{bo} + W_{ho} + W_{30})/2 \qquad (53)$$

$$+\sqrt{\left(\frac{W_{bo} + W_{ho} + W_{30}}{2}\right)^2 + W_3\left(\frac{t_{ho}\xi}{t_h}\right)^6\left(\frac{W_c}{W_{co}}\right)^2 W_T}$$

4. RELATED INVESTIGATIONS

Three investigations related to the HIM meteoroid shield development effort were carried out which treated subjects that may influence the design of the HIM vehicle, but were not limited to the HIM spacecraft dust shield. The first examined the use of Kevlar/epoxy composites in place of homogeneous metal for the bumper and front surface of the underlying structure of a 2-layer meteoroid shield system. The second study examined the meteoroid impact response of mirrors to be extended into the meteoroid stream as the HIM vehicle approaches Halley's Comet. The third study examined the formation and propagation of an ion field surrounding the HIM vehicle that is produced by meteoric impacts on the vehicle shield. Brief resumes of each of these studies are presented in this chapter. Original (and more complete) treatments of these studies were submitted to JPL in the form of informal memoranda during conduct of the investigation.[18,19,20]

4.1 USE OF KEVLAR CLOTH/EPOXY PANELS IN METEOROID SHELDS FOR HALLEY'S COMET INTERCEPT VEHICLE

The original concept for the Halley's intercept mission involved transporting a variety of instruments for determining the chemistry of material emitted from the comet in the form of both gas/plasma and small meteoroids. These experiments are sensitive to materials typically found in organic compounds such as carbon, oxygen, nitrogen, etc. For this reason, a vehicle design criterion was established that: no organic materials could be exposed to meteoroid fluxes which would produce vapor/plasma. Tests conducted by Earnst Mach Institute (EMI) for the development of the Europeon Space Agency (ESA) Halley encounter mission spacecraft [17] revealed that Kevlar/epoxy panels may have certain advantages over the aluminum panels for meteoroid armor when used as either the meteoroid bumper or facing for the underlying structure.

The importance of these discoveries for the HIM vehicle development effort increased markedly when new vehicle concepts were considered that did not involve on-vehicle chemistry experiments

(thus eliminating the need for excluding organic materials from meteoroid exposure). An abbreviated effort was conducted to determine potential for using organic materials in the HIM vehicle shield. Panels made from Kevlar/epoxy matrices were identified as having the greatest performance capability of any organic composite due to their exceptional strength-to-weight ratios and their proven impact toughness.

4.1.1 Fibrous Bumper Material

The EMI experiments found that Kevlar/epoxy panels with masses-per-unit-areas equal to optimum aluminum panels produced debris clouds with nearly the same damage potential to underlying structures as those produced by their aluminum bumper counterparts. The physical thicknesses of these panels were approximately twice those of the denser aluminum material. The investigators noted that the total area on the bumper disrupted by the impact on the bumper were greater than those for aluminum bumpers, but that the majority of this disruption involved debonding the Kevlar fibers from the epoxy substrate. These fibers expanded laterally thereby partially blocking the hole which would otherwise have been produced by the primary impact. Reducing such hole diameters has potential for significantly reducing the danger of primary meteoroid impact onto the front face of the underlying structure.

This concept was investigated theoretically by producing a simple model which suggests that the Kevlar fibers would expand one bumper plate thickness into the hole, thus reducing the hole diameter by twice the plate thickness. The size of a meteoroid with a 50% probability of passing through the front plate of a structure exposed to a typical Halley's Comet environment was reduced from 3×10^{-4} m dia. to 6×10^{-5} m dia. by the simple expedient of replacing the aluminum bumper with an equivalent one made from Kevlar/epoxy composite. In addition, the Kevlar bumper can be made structurally more rigid than the aluminum bumper by virtue of its greater thickness. This greater rigidity reduces the size and number of

structural supports needed to support it thus reducing the danger to the vehicle from particles emanating from an impacted hard point at or near the bumper surface.

Finally, the bumper material that can be launched as individual fragments consists of finely divided epoxy powder and short lengths of fine Kevlar fibers. Both of these materials have negligible impact damage potential for underlying structures thus effectively eliminating one of the four mechanisms identified as threats for 2-layer meteoroid armor.

4.1.2 Kevlar Face Plates for Underlying Structures

The experiments conducted at the EMI concluded that aluminum facing material for aluminum honeycomb sandwich was more effective than Kevlar if the same thickness of Kevlar were substituted. The situation was reversed if the same mass-per-unit area of Kevlar were substituted (approximately twice the thickness of the aluminum sheet). We suggest that the explanation for this result involves our approximation that the front face of the underlying honeycomb sandwich structure has zero strength and rigidity. Such a panel transfers much impulse delivered to the front surface to the honeycomb immediately behind where it is absorbed. The situation becomes far more complicated but more benign structurally when the front surface of the honeycomb panel is allowed significant rigidity and strength. Part of the impulse may be transferred laterally away from the original impact site where it can be borne by surrounding areas of honeycomb and by other supports for the front surface. The problem of predicting such behavior mathematically is formidable and probably requires use of dynamic finite-element computer codes. The greater thickness of the Kevlar material renders it significantly more rigid than the aluminum and, therefore, more agile at transferring impulse laterally. Experiments conducted where the facing plate was divided and the gap filled with a mylar thermal blanket (approximately 1 cm thick in its uncompacted state and less than 1 mm thick when fully compacted) could produce no visible signs

of honeycomb damage. This result produced considerable surprise. After some consideration we decided that it represented a continuation of the structural rigidity argument discussed earlier. The dual plates separated by a very soft spring tend to aid the process of lateral distribution of impulse thus protecting the underlying structure from damage. Since no damage was produced to the honeycomb on-axis, the experiments provide only a lower bound upon the extent of damage reduction (and hence impulse intensity reduction) that can be achieved by separating the rear plate into multiple layers.

We concluded from the study that the use of Kevlar epoxy panels for both bumpers and substrate facing structures open exciting possibilities for achieving significant size and weight reductions of meteoroid armor systems. The technology in this area is young and requires considerably more experimental and theoretical work before it can be exploited effectively.

4.2 MIRROR EXPOSURE DYNAMICS

One important requirement for the Halley's intercept mission was to observe the comet for as long a time as possible during the approach phase of the maneuver, first to provide detailed orbit ephemeris and navigational information and then to observe its structure and surface condition. Cameras mounted on the HIM vehicle are set to "look" outward from the side of the vehicle. A small mirror mounted adjacent to the objective lens but behind the shield allows the camera view-field to be turned to look nearly, but not quite, forward. An outboard mirror was also to be available which allowed the area directly ahead of the vehicle to be observed. This mirror must be mounted beyond the shield and hence exposed to meteoroid flux. The outboard mirror would be jettisoned when the HIM vehicle was close enough to Halley's Comet so that the comet could be observed through use of the inboard mirror when the vehicle was oriented properly to achieve protection from the shield. The question addressed in the study was, "How much damage is the outboard

mirror likely to sustain before it is jettisoned?"

We started the analysis by considering a glass mirror. Hypervelocity impacts onto rigid brittle material such as glass produce conventional hemispherical craters, but they also produce front spall zones which extend outward from the bottom floor of the crater and terrace upward toward the original surface until they intersect the surface some distance beyond the crater lip. Impact data from laboratory experiments conducted at velocities between zero and 7.5 km/s indicated that the ratio of the calculated hemispherical crater diameter to front spall diameter increases linearly with velocity. Extrapolation of this relationship to velocities associated with Halley's Comet intercepts leads to the prediction that craters with aspect ratios near 60 would be produced. Such craters would remove the mirror surface 60 times over during a vehicle approach from great distance to 2500 km from Halley's Comet. We decided somewhat arbitrarily to truncate the expansion of the crater aspect ratio at an extrapolated impact velocity of 15 km/s and allow it to remain constant as velocities increased beyond that point. Application of this approach indicated that more than 60% of the mirror surface would be removed. This result also is clearly unacceptable. A conclusion from this analysis was that glass is an unacceptable surface material for such an outboard mirror application.

We next turned our attention to mirrors made from relatively ductile metals that do not suffer from front spall phenomena. Unfortunately, such materials suffer from phenomena probably related to front spall. The surface surrounding an impact crater in ductile metal is heaved upward and is wrinkled. The extent of this upward heave has never been measured precisely, but it is obvious out to distances of at least 1 crater diameter beyond the crater in all directions. This upheaval is doubly disadvantageous to mirror operation since: it both eliminates the mirror surface from effective image formation; and it provides significant areas of mirror surface whose angle is only slightly different from the

desired angle. Light reflected from these surfaces is imaged by the camera optics to form halos around bright objects being viewed thereby reducing contrast and spacial resolution of the resulting images to an extent even greater than that produced by simple removal of mirror surface. Therefore, we anticipate serious mirror degradation even though only 7.2% of the surface is expected to be occupied by craters.

Another problem with the use of thick aluminum mirrors is that they produce aluminum vapor and plasma during exposure to meteoroid fluxes. The mirror specified for the Halley's Comet mission may produce as much as 2 to 3 grams of aluminum vapor/plasma before it is jettisoned. Much of this plasma is projected inboard toward the vehicle where it can coat optical components, electric insulators, sensors, solar cells, etc.

We propose two solutions to the dilemma of not being able to use conventional mirror materials. First, the size of the outboard mirror can be reduced sharply if it is articulated to provide camera scan capability. A shutter is also required over the mirror so that it can be exposed to the flux for periodic "peaks" during the approach phase of the mission.

Another approach is to use an aluminized membrane as a mirror surface. The hole diameters in the membrane are confined to near those of the meteoroids themselves for larger meteoroids and a 10 μm thick membrane is expected to lose only 2.1% of its surface during exposure to the meteoroid field. A basic problem with membrane mirrors is their propensity for vibration. A means for damping this vibration by connecting the membrane to an underlying structure with elastomeric mounts might be effective in damping such oscillations. We feel, that, while adventurous, this technology bears careful consideration. Its feasibility can be investigated with currently available facilities.

4.3 EVALUATION OF ION FIELDS PRODUCED AROUND THE HIM VEHICLE BY METEOROID IMPACTS

A potential problem exists that ionization produced by impacts of meteoroids and plasma upon the HIM vehicle may produce a cloud surrounding the vehicle that is intense and extensive enough to affect microwave transmission between the vehicle and Earth. In principle, this is not a devastating problem for the HIM vehicle since it can store data gathered for later transmission when it is no longer subjected to severe bombardment. The Giotto vehicle, currently being developed by the European Space Agency for travel to Halley's Comet, has a significantly more severe problem in this area because it is designed to return observations in real time and to cease functioning shortly after it passes Halley's Comet.

We started the analysis of this problem by generating very simple models to describe the number of ions produced during meteoroid bombardment and the average velocity with which these ions recede from the vehicle after production. We used these models to calculate electron (ion) concentrations vs. distance from the vehicle during the periods of maximum bombardment intensity (closest approach to the comet). We also established the range from the vehicle where the expanding ion cloud would be significantly affected by plasma/debris interactions. The results of this study have been used to indicate that, at worst, the plasma from meteoric impact provides electron concentrations along a line-of-sight to Earth equal to electron concentrations in the ionosphere around Earth. Communications specialists have indicated that such concentrations do not constitute a severe limitation upon communications.

REFERENCES

1. Sekanina, Z., "Expected Characteristics of Large Dust Particles in Periodic Comet Halley". Proceedings of Comet Halley Micrometeoroid Hazard Workshop. European Space Agency, ESA SP-153, April 1979, pps. 25-34.

2. Divine, N., "Numerical Models for Halley Dust Environments." Proceedings of Comet Halley Dust and Gas Environments Workshop. European Space Agency, ESA SP-174, November 1981, pp. 25-30.

3. Newburn, R. L., "Physical Models of Comet Halley Based Upon Qualitative Data from the 1910 Apparition". Proceedings of Comet Halley Micrometeoroid Hazard Workshop. European Space Agency, ESA SP-153, April 1979, pps. 35-50.

4. Swift, H. F., and A. K. Hopkins, "Effects of Bumper Material Properties on the Operation of Spaced Meteoroid Shields", Journal of Spacecraft and Rockets, Vol. 7, No. 1, pps. 73-77.

5. Cour Palais, B. G. and Frost, V., "Empirical Hypervelocity Equations Developed for Project Apollo" Proceedings of the OART Meteroid Impact and Penetration Workshop; NASA Manned Spacecraft Center, October 8, 9, 1968.

6. Cour Palais, B. G., "Space Vehicle Meteoroid Shielding Design", Proceedings of Comet Halley Micrometeoroid Hazard Workshop, European Space Agency, ESA SP-153, April 1979.

7. Personal Communication (to H. F. Swift) by Dr. E. Schnider, Earnst Mach Institute, Freiberg, F.R.G.

8. McMaster, W. H. et. al., "Compilation of X-Ray Cross Sections, Lawrence Livermore Laboratory" Report UCRL-50174, Sec. 2, May, 1973.

9. Wagner, M. H.; Kreyenhagen, K. N., "Review of Hydroelastic Plastic Code Analyses as Related to the Hypervelocity Particle Impact Hazard", Proceedings of the Comet Halley Micrometeoroid Workshop, European Space Agency,ESA SP-153, April 1979, pps. 115-121.

10. Kinslow, R. (Editor), "High Velocity Impact Phenomena", Academic Press, New York City, N.Y., 1970

11. Swift, H. F.; et. al., "Characterization of Debris Clouds Behind Impacted Meteoroid Bumper Plates", Proceedings of the AIAA Hypervelocity Impact Conference, Cincinnati, Ohio, May 1969, AIAA Paper, 69-380.

12. Swift, H. F., "Protecting the EEC Comet Halley Probe From Meteoroid Impact." Proceedings of the Comet Halley Micrometeoroid Hazard Workshop, European Space Agency, April 1979, ESA SP-153, pp. 67-72.

13. McFarland, R. C. Jr., "A Limit Analysis of the Collapse of Hexagonal Cell Structures Under Axial Load", JPL Technical Report 32186, December 1, 1961 (JPL internal document).

14. Carson, J. M.; Hopkins, A. K., "Impact Response of High Strength, Carbon Fiber/Epoxy Composite Materials." Air Force Materials Laboratory Technical Report AFML-TR-71-178, October 1971.

15. Zucas, J. A., et. al., "Impact Dynamics", John Wiley & Sons New York City, February 1982.

16. Swift, H. F. et. al., "Debris Clouds Behind Plates Impacted by Hypervelocity Pellets". Journal of Spacecraft and Rockets, Vol. 7, No. 3, March 1970.

17. Reinhard, R., "The Giotto Project - A Fast Flyby of Halley's Comet", European Space Agency (ESA) Journal, 1981, Vol. 5 pp. 273-285.

18. Swift, H. F., "Use of Kevlar Cloth/Epoxy Panels in Meteoroid Shields of Halley Comet Intercept Vehicle", Memorandum to R. Chen, Applied Mechanics Technology Section, JPL, July 30, 1981 (JPL internal document).

19. Swift, H. F., "Outboard Mirror For HIM Camera", Memorandum to R. Chen, Applied Mechanics Technology Section, JPL, February 12, 1981 (JPL internal document).

20. Swift, H. F., "Ion Concentration from Meteoroid Impacts Against HIM Vehicle Near Halley's Comet". Memorandum to R. Chen, Applied Mechanics Technology Section, JPL, April 2, 1981 (JPL internal document).

21. Richardson, A.J., "Theoretical Penetration Mechanics of Multisheet Structures Based on Discrete Debris Particle Modeling", AIAA Hypervelocity Impact Conference, Cincinnati, Ohio, April-May, 1969. AIAA Paper No. 69-371.

C-2